MRI & MRS assessment of the role of the tumour microenvironment in response to therapy

Leanne K. Bell[a]*, Nicola L. Ainsworth[a], Shen-Han Lee[a] and John R. Griffiths[a]

MRI and MRS techniques are being applied to the characterisation of various aspects of the tumour microenvironment and to the assessment of tumour response to therapy. For example, kinetic parameters describing tumour blood vessel flow and permeability can be derived from dynamic contrast-enhanced MRI data and have been correlated with a positive tumour response to antivascular therapies. The ongoing development and validation of noninvasive, high-resolution anatomical/molecular MR techniques will equip us with the means to detect specific tumour biomarkers early on, and then to monitor the efficacy of cancer treatments efficiently and reliably, all within a clinically relevant time frame. Reliable tumour microenvironment imaging biomarkers will provide obvious advantages by enabling tumour-specific treatment tailoring and potentially improving patient outcome. However, for routine clinical application across many disease types, such imaging biomarkers must be quantitative, robust, reproducible, sufficiently sensitive and cost-effective. These characteristics are all difficult to achieve in practice, but image biomarker development and validation have been greatly facilitated by an increasing number of pertinent preclinical *in vivo* cancer models. Emphasis must now be placed on discovering whether the preclinical results translate into an improvement in patient care and, therefore, overall survival. Copyright © 2011 John Wiley & Sons, Ltd.

Keywords: tumour microenvironment; therapy; treatment; response

INTRODUCTION

Tumour development involves the gradual accumulation of somatic mutations by cells to produce a heterogeneous malignant population. However, in recent years, this definition has been recognised as an oversimplification of a far more complicated process (1). It is now known that tumour cells rely on their immediate surrounding environment for structural support, signalling and nutrition, and, in some cancers, non-neoplastic cells may account for up to 90% of the total tumour mass. Tumour progression therefore depends on complex interactions between malignant tumour cells (most often of epithelial derivation), which are embedded within an abundance of stromal elements including fibroblasts and stromal deposits (forming the extracellular matrix (ECM)), and a variety of bone marrow-derived cells (2). Together, these components form a sophisticated unit, commonly known as the tumour microenvironment (TME) (Fig. 1).

The role of the TME in cancer propagation, invasion and metastasis has already been extensively reviewed (3–7). However, only recently has interest arisen with regard to how interactions between specific components of the TME, whether cell–cell or cell–ECM, are integral in the regulation and facilitation of carcinogenesis. In some contexts, the tumour cells themselves influence the TME, such that a fully functioning 'cancer organ' is emulated (1). Membrane-type matrix metalloproteinase-1, the best-characterised membrane-anchored matrix metalloproteinase (MMP) (8), is expressed on both tumour and stromal cell surfaces (9,10), and therefore exemplifies the importance of cell–ECM interactions in the manifestation of the TME.

Although this review is primarily concerned with the use of MR in probing the TME, we also address research concerned with TME–tumour cell interactions. MR has long been applied to the elucidation of tumour properties and, over recent years, there have been a number of excellent reviews detailing past achievements and recent advances in the field of MRI and MRS characterisation of the TME (11–14). Researchers are now exploiting

* Correspondence to: L. K. Bell, Cancer Research UK, Cambridge Research Institute, Li Ka Shing Centre, Robinson Way, Cambridge, CB2 0RE, UK.
E-mail: leanne.bell@cancer.org.uk

a L. K. Bell, N. L. Ainsworth, S.-H. Lee, J. R. Griffiths
Cancer Research UK, Cambridge Research Institute, Li Ka Shing Centre, Cambridge, UK
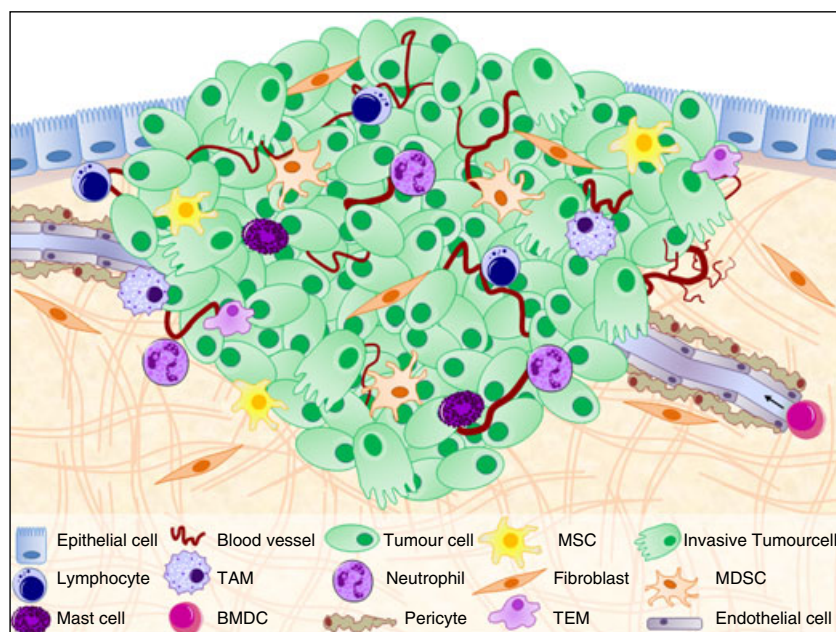

Figure 1. The tumour microenvironment (TME). The primary TME involves a complex interplay between malignant tumour cells and numerous host cell types, including endothelial cells of the blood circulation, stromal fibroblasts and a variety of bone marrow-derived cells (BMDCs), including tumour-associated macrophages (TAMs), myeloid-derived suppressor cells (MDSCs), TIE2-expressing monocytes (TEMs) and mesenchymal stem cells (MSCs). The extracellular matrix consists of stromal deposits which, together, form a scaffold that supports the cells of the TME. Invasive tumour cells may subvert the basement membrane to permit invasion, metastasis and a consequent systemic spread of the disease. Based on Nat. Rev. Cancer, 9, 239–252, copyright 2009, by permission from Macmillan Publishers Ltd.

various MR techniques to target specific aspects of the TME (Table 1) and, ultimately, to identify biomarkers for the noninvasive measurement of TME response to therapy *in vivo*, reproducibly, in real time and with minimal side-effects.

In this review, we highlight recent examples to illustrate this point and the wide-ranging applications of MR currently being applied to the TME, with a focus on emerging MR methods that may in future be used in the clinic to measure tumour and TME response to targeted chemotherapeutics. We begin by briefly describing passive and actively targeted MRI contrast agents currently used in widespread preclinical and clinical research. We continue by reporting on the many and varied MR-based methods which are being applied to characterise specific aspects of the TME, namely pH, oxygenation, temperature, metabolites, water mobility and pressure, and the ECM, and assess how established imaging biomarkers alter in response to therapy.

CONTRAST AGENTS AS PROBES OF THE TME – PASSIVE AND ACTIVE MECHANISMS

MRI can be enhanced by a range of intravenously administered contrast agents, which we introduce briefly here before describing selected applications. These agents are all extracellular, so that they can, in general, be regarded as probes of the TME. It is also possible to engineer these agents to bind specific molecules and improve their specificity. MRI contrast agents fall broadly into two classes: positive contrast (which shorten water T_1 and cause brightening of T_1-weighted images), typically consisting of chelated gadolinium ions, and negative contrast (which shorten water T_2 and T_2^*, causing darkening of T_2- or T_2^*-weighted images), a typical example being magnetic nanoparticles (MNPs), such as coated

superparamagnetic iron oxide (SPIO) particles (12). Their intravascular lifetime varies from minutes (for small gadolinium chelates) to hours (for some SPIO particles or gadolinium chelates attached to larger molecules). Their effect may be measured by comparing images pre- and post-contrast administration (sometimes up to 24 h later in the case of targeted agents to allow clearance of unbound agent), or by dynamic measurements of the signal change after the agent has been administered, allowing the assessment of parameters relating to blood flow, volume and vessel permeability.

In dynamic contrast-enhanced MRI (DCE-MRI), low-molecular-weight (<1000 Da) contrast agents are administered intravenously, and rapidly diffuse from the tumour vessel lumen to the extracellular extravascular space along a concentration gradient. The resulting change in water T_1 leads to changes in signal intensity (SI) that can be used to calculate the contrast agent concentration, and can then be pharmacokinetically modelled, providing quantitative information reflecting tumour microvessel perfusion, permeability and extracellular leakage characteristics (15,16). The pros and cons of DCE-MRI data processing have been covered extensively elsewhere (15,17–20).

Although gadolinium-based agents are in widest use in MRI, there is also considerable interest in MNPs, both as MRI contrast agents and as carriers for targeted drug delivery. In simple terms, MNPs consist of an inorganic nanoparticle core and a biocompatible surface coating, to which can be added functional ligands targeted to components of the matrix or to cell surface markers. An excellent review on the design of MNPs has been published by Veiseh *et al.* (21). The properties of MNPs can be altered by their surface coating, shape and size, allowing specific tailoring to the target. Functional ligands, such as targeted agents, therapeutics or optical dyes, can be added to

Table 1. MR techniques for monitoring tumour microenvironment (TME) response to therapy

TME target	MR technique	Example(s)
Vasculature	DCE-MRI	(32–35,40)
	Susceptibility- weighted contrast MRI	(39,40,42)
	Vessel size index MRI	(41)
	Targeted MRI contrast agents	(45–52)
	DWI	(36,166,167,192)
Oxygenation	DCE-MRI	(103,114)
	BOLD	(106–109,112–115)
	TOLD	(105)
	OMRI	(145,146)
	FREDOM	(109,129)
	^{1}H MRS/^{19}F MRI	(116,117,126)
	^{19}F MRS	(118–122,127,130–135,137–139)
	EPR oximetry	(141,144)
Extracellular pH	^{1}H MRSI	(72–74)
	^{13}C MRSI	(82)
	MR-PET	(194)
Temperature	MR thermometry	(97–100)
Extracellular matrix	Targeted MRI contrast agents	(30,168,169,170,172)
	'Smart' MRI contrast agents	(178,181–186)
	MTI	(188,189)
	CEST	(190,191)
	$T_{1\rho}$	
Interstitial fluid pressure	DCE-MRI	(149,153–155)
	Contrast-enhanced MRI	(152)
Stromal cells	Contrast-labelled stromal cells	(171)
Immune cells	Contrast-labelled immune cells	(53–57)

BOLD, blood oxygen level-dependent; CEST, chemical exchange saturation transfer; DCE-MRI, dynamic contrast-enhanced MRI; DWI, diffusion-weighted imaging; EPR, electron paramagnetic resonance; FREDOM, fluorocarbon relaxometry using echo planar imaging for dynamic oxygen mapping; OMRI, Overhauser-enhanced MRI; PET, positron emission tomography; TOLD, tissue oxygen level-dependent.

the surface or incorporated into the MNP (21). The attachment of targeted agents to MNPs increases the concentrations of contrast agent within a target tissue and increases the signal-to-noise ratio (SNR) for improved detection by MRI. Active targeting can be achieved using ligands such as proteins, small molecules or antibody–antigen interactions. MNPs have great potential to be multifunctional, combining targeted drug delivery with real-time monitoring of drug delivery and assessment of efficacy of therapeutic intervention. The combination of drug delivery and MRI contrast agent could be highly clinically significant. A number of groups have used MNPs for the targeting of drug delivery to cancer cells; examples include cisplatin, paclitaxel, doxorubicin and methotrexate (22–24). Jain *et al.* (25) showed that the incorporation of doxorubicin and paclitaxel with MNPs did not alter significantly the MRI characteristics of the contrast agent *in vivo*, and that the drugs still had significant antiproliferative effects in MCF-7 breast cancer cells. Kohler *et al.* (22) evaluated methotrexate conjugated to an MNP in 9L glioma cells. They reported uptake, enhancement on MRI and increased cytotoxicity compared with unconjugated methotrexate. However, the *in vivo* analysis of imaging and response with this combination has not been conducted. In addition to chemotherapy, gene therapy with small interfering RNA (siRNA) has shown promise. Medarova *et al.* (26) used an MNP probe for siRNA delivery and imaging, and found that

it silenced green fluorescent protein (GFP) production in a GFP-expressing xenograft tumour, and increased the levels of apoptosis. This study used a second probe to assess necrosis in another xenograft model; this was achieved by targeting the anti-apoptotic birc5, which encodes survivin, an inhibitor of apoptosis, to assess necrosis in a xenograft model. Simultaneous delivery and detection of siRNA and gene silencing were shown *in vivo*. Future challenges in the design and use of MNPs for imaging *in vivo* include the ability to overcome biological barriers, such as the blood–brain barrier, and the evasion of detection and clearance by the reticuloendothelial system, as well as the development of tailored agents for the monitoring of each specific therapy.

The targeting of molecular MRI contrast agents to biomarkers within the TME is a promising noninvasive technique for the assessment of the efficacy of anticancer therapies *in vivo*. Preclinically, these agents have detected a range of cell type-specific- and generic biomarkers of the TME, whilst successfully exploiting the high-resolution anatomical and molecular information available with MRI. Selectively targeted contrast agents have been designed to bind molecules of the TME and also extracellular targets on the tumour cell surface which mediate cell–TME interactions (Table 2). By developing new methods to improve SNR (which may depend on the accumulation of a higher concentration of targeted contrast agent per voxel), the suitability of target-specific MRI contrast agents for clinical application may

Table 2. Examples of targeted contrast agents for MRI of the tumour microenvironment

Contrast agent target	Contrast agent complex	Targeting molecule	Contrast moiety	Validation and conclusions	
Tumour ECM targets					
Type I collagen					
An abundant component of the ECM and fibrosis	EP-3533	Cyclic 10-amino-acid peptide with three primary amine groups for appendage of contrast moiety	Gadopentetate dimeglumine (three moieties per peptide)	Dynamic T_1-weighted MRI was performed at 4.7T in the presence of EP-3533. Data demonstrated accurate differentiation between densely collagenous scarred myocardium and blood, and between normal myocardium and scarred myocardium in a mouse model of healed post-infarction myocardial scarring	(169)
Hyaluronidase					
A biomarker of angiogenesis and metastasis in ovarian carcinoma. Its substrate, hyaluronan, is a component of the ECM, important in maintaining tissue architecture	Hyaluronan–GdDTPA beads	Hyaluronan	GdDTPA	Significant increases in R_1 were observed (most apparent at 2.5 min post-contrast) in human ES-2 ovarian xenografts grown in nude mice. Significant increases in R_1 were attributed to hyaluronan–GdDTPA bead-mediated detection of hyaluronidase activity in the vicinity of the xenografts	(168)
Fibrin/fibronectin					
Components of the ECM, fibrosis and blood clotting. Tumour stromal fibronectin is also associated with angiogenesis	CTL1–(GdDTPA)	CTL1 cyclic decapeptide (conjugated to contrast moiety at N-terminus)	GdDTPA	Maximal enhancement was observed 60 min post-contrast in female athymic (nu/nu) mice bearing human HT-29 colon carcinoma xenografts. Administration and competitive binding of free CTL1 peptide reduced contrast-induced enhancement. CTL1–(GdDTPA) demonstrated specific targeting of fibronectin–fibrin complexes in HT-29 xenografts with minimal binding to normal tissues. MRI data were corroborated with ex vivo histological staining for fibronectin	(30)
Matrix metalloproteinase (MMP)					
Potential biomarker for cancer progression,	PCA2-switch	MMP-2 peptide substrate linked to contrast moiety	GdDOTA	At 40 min post-contrast, an increase in R_1 was induced by PCA2-switch in wild-type	(172)

(Continues)

Table 2. *(Continued)*

Contrast agent target	Targeting molecule	Contrast agent complex	Contrast moiety	Validation and conclusions
invasiveness, angiogenesis and metastasis (e.g. hepatocellular carcinoma)	via a 12-carbon alkyl chain			mouse MC7-L1 mammary carcinoma xenografts. The increase in R_1 was attributed to cleavage of PCA2-switch by MMP-2 and accumulation of the agent in the wild-type tumour. This study constitutes the first example of detection of MMP-2 activity *in vivo* by MRI
(Tissue) Transglutaminase				
A multifunctional GTP–GDP-binding enzyme which contributes to stabilisation of the ECM and cell–substrate interactions. Associated with many cellular processes and implicated in fibrosis and metastasis	Transglutaminase substrate (TGS) (hexameric peptide from α2 plasmin inhibitor human gene)	TGS–GdDTPA	Lysine–GdDTPA linked to the TGS at its C-terminus	R_1 maps demonstrated significant increase in relaxation rate in human MCF7 breast carcinoma spheroids (≤1.0 mm in diameter) following contrast administration. R_1 histograms demonstrated a shift to the right in the presence of TGS–GdDTPA. These changes were attributed to tissue retention of TGS–GdDTPA as a result of cross-linking of TGS by endogenous transglutaminase (170)
Fibroblasts				
Stromal cell instigators of tumour desmoplasia. Matrix-bound fibroblasts are associated with angiogenesis and endothelial cell motility. Potential biomarker for angiogenesis and tumour progression	PFN2 fibroblasts (obtained from a poorly differentiated invasive G3 breast tumour)	Biotin–BSA–GdDTPA-labelled fibroblasts	Biotin–BSA–GdDTPA (incubated with fibroblasts *in vitro* for 48 h)	R_1 values were significantly elevated in human MLS ovarian carcinoma xenografts both 1 and 8 days following inoculation with labelled fibroblasts. Significantly increased contrast persisted for ≥8 days *in vivo*. MRI data demonstrated local and systemic recruitment of fibroblasts to the rim of the xenografts and corresponded with localisation of tortuous vasculature. These results provide dynamic evidence for the role of fibroblasts in the maintenance of functional tumour vasculature and offer a means of image-guided targeting of these abundant stromal cells to the tumour as a potential mechanism for cellular cancer therapy (171)

(Continues)

Table 2. (Continued)

Contrast agent target	Contrast agent complex	Targeting molecule	Contrast moiety	Validation and conclusions	
Tumour vasculature targets					
Endoglin (CD105)					
Co-receptor of the TGF-β superfamily, largely expressed in small and (probably) immature tumour vessels as demonstrated in breast, prostate and gastric cancers as well as gliomas. Biomarker of tumour angiogenesis	CD105-Gd-SLs	(MPB)-anti-CD105 mAb	Sterically stabilised GdDTPA liposomal nanoparticles	F98 glioma cell xenografts (grown in rats) challenged with CD105-Gd-SLs demonstrated signal enhancement which increased up to 60 min post-contrast. A further increase in signal was observed at 120 min post-contrast and correlated with increased expression of CD105 as determined histologically. Signal enhancement resulted from Gd^{3+} binding to CD105 on new vessels, yielding signal specifically from angiogenic sites	(51)
$\alpha_v\beta_3$- integrin					
Established biomarker of angiogenesis which is relatively selective for activated endothelial cells, but unexpressed on mature and quiescent cells	$\alpha_v\beta_3$-targeted paramagnetic nanoparticles	$\alpha_v\beta_3$-targeted peptidomimetic antagonist (covalently coupled to the surfacant co-mixture)	GdDTPA-BOA	Contrast agent administration to rabbit VX-2 xenografts caused a marked initial increase in T_1 signal intensity at the tumour periphery, consistent with the predominant distribution of angiogenesis as demonstrated histologically. At 2 h post-contrast, the signal increase was 56% compared with nontargeted control nanoparticles. These data demonstrate the potential of the contrast agent for the detection and characterisation of neovasculature, and for assessing the effectiveness of antiangiogenic treatment regimes	(195)
				T_1-weighted MRI data were acquired for human C-32 melanoma xenografts up to 120 min post-contrast. Contrast enhancement of neovascularity was 173% by 120 min post-contrast, which was ~50% greater than nontargeted control nanoparticles. This study lowers the previously reported limit for detection of sparse neovascular biomarkers *in vivo* at clinically relevant field strengths	(47)

(Continues)

Table 2. *(Continued)*

Contrast agent target	Contrast agent complex	Targeting molecule	Contrast moiety	Validation and conclusions	
	RGD-pQDs ($\alpha_v\beta_3$-integrin targeted multimodal quantum dots (QDs))	RGD $\alpha_v\beta_3$-integrin tripeptide (conjugated to quantum dots with a paramagnetic coating)	GdDTPA-BSA [GdDTPA-*bis*-(stearylamide)]	T_1-weighted MRI data were acquired both pre- and post-contrast in mouse B16F10 melanoma xenografts. Significant signal enhancement following RGD-pQDs was found mainly at the tumour periphery, corresponding to those regions with highest angiogenic activity, as determined by fluorescence microscopy. These data demonstrated that visualisation of angiogenesis can be achieved at anatomical resolutions, and RGD-pQDs represent a novel means of assessing many pathophysiological processes *in vivo*	(50)
CD13 (aminopeptidase N isoform)					
Transmembrane glycoprotein involved in cancer angiogenesis, tumour invasion and metastasis, and which is highly expressed on activated endothelial cells of tumour vasculature. Biomarker for tumour angiogenesis	cNGR-pQDs (cyclic Asn–Gly–Arg is a tumour-homing tripeptide and ligand of CD13)	cNGR (biotinylated and attached to avidin-coated quantum dots)	GdDTPA (biotinylated in a wedge and attached to avidin-coated quantum dots)	Contrast agent was administered to Swiss nu/nu mice bearing human LS174T colorectal carcinoma xenografts. For cNGR-labelled and unlabelled pQDs, ΔR_1 was spatially heterogeneous throughout the tumour post-challenge, but most pronounced at the tumour rim. Although an R_1 increase was observed for unlabelled pQDs, the average response was three-fold lower compared with cNGR-pQDs. The presented results designate cNGR as an effective ligand for discriminating between quiescent and activated endothelium and for quantifying the extent of tumour angiogenic activity *in vivo*	(52)
Tumour-associated immune cell targets					
Her-2/neu receptor-targeted natural killer (NK) cells					
NK cells were targeted to the Her-2/neu tumour cell surface receptor. Her-2/neu is involved in signal transduction pathways	Ferumoxtran-labelled anti Her-2/neu directed NK-92-scFv(FRP5)-zeta cells	NK-92-scFv(FRP5)-zeta cells (genetically engineered NK cells which specifically and efficiently lyse Her-2/neu-expressing tumour	Ferumoxtran (second-generation SPIO)	MRI data were acquired pre- and post-administration of ferumoxtran- labelled, Her-2/neu-targeted NK cells to nude Balb/c-AnNCrl mice bearing Her-2/neu-positive NIH 3T3 mammary carcinoma	(54)

(Continues)

Table 2. (Continued)

Contrast agent target	Contrast agent complex	Targeting molecule	Contrast moiety	Validation and conclusions	
leading to cell growth and differentiation, is overexpressed in many human tumour types of epithelial derivation (such as breast, stomach, gastric and endometrial carcinomas) and is linked with cancer development and progression. Her-2/neu is therefore a biomarker for tumour aggressiveness and is associated with poor prognosis in breast cancer		cells and delay tumour growth)		xenografts. A significant decrease in tumour signal-to-noise ratio was observed in response to contrast agent. Immunohistochemistry confirmed accumulation of labelled NK cells in xenografts. This method represents a means of monitoring NK cell homing and engraftment in human tumours, but further studies are warranted to investigate contrast agent pharmacokinetics and elimination before clinical implementation	
Dendritic cells (DC)					
DCs migrate to the lymph nodes to present their antigen to resident T-cells. DCs are professional antigen-presenting cells and have been shown to trigger specific anti-tumour immunity (181). Tumour antigen-loaded DC vaccines have been introduced in the clinic with some success, but limited effective immune induction, possibly as a result of inefficient delivery to lymph nodes.	Ferumoxide-labelled, antigen-pulsed DC vaccine	Melanoma antigen-pulsed, DC vaccine generated from adherent peripheral blood mononuclear cells	Ferumoxide SPIO (added at 200 μg/mL, 3 days after commencement of DC culturing and prior to DC maturation)	Eight stage-III melanoma patients received the SPIO-loaded DC vaccination by intranodal injection on day 0. On day 2, in vivo MRI (3T) was conducted, followed by ex vivo MRI (7T) of dissected lymph nodes. Pre- and post-cell injection T_2^*-weighted MGRE in vivo MRI demonstrated a significant decrease in signal intensity at the injection site. Turbo SE images enabled localisation of the signal decrease to the lymph node. An excellent correlation was seen between hypointense areas on ex vivo MRI and regions containing large numbers of SPIO-positive cells (as determined histologically). This study demonstrates the potential use of MRI for tracking therapeutic cells in vivo	(53)
Advantageously, immature DCs naturally endocytose certain contrast agent labels in substantial amounts (49)	Gd-contrast agent-labelled DCs	DCs (iDCs) cultured from rat bone marrow	Prohance (Gd(II)-HP-DO3A) (added at 25 mM, 6 days after commencement of	Initially, T_1- and T_2- weighted MRI were conducted for localisation of 9L glioma rat brain xenografts. Control or Gd-contrast agent-labelled DCs were injected	(56)

(Continues)

Table 2. *(Continued)*

Contrast agent target	Contrast agent complex	Targeting molecule	Contrast moiety	Validation and conclusions	
			DC culturing and prior to DC maturation)	intratumorally and the imaging protocol was repeated within 30 min of DC administration. The percentage contrast enhancement (%CE) was calculated using the pre- and post- DC MRIs. A significant difference was observed between %CE of tumour injected with labelled DCs *versus* tumours injected with untreated DCs. Labelling had no apparent effect on interactions between DCs and NK cells. This work supports the continued development of Prohance as a means of labelling immune cells to monitor their delivery, trafficking and localisation	
Tumour-associated macrophages (TAMs)					
TAMs invade the tumour stroma in many cancers, participating in tumour invasion, angiogenesis and metastasis formation, and are therefore associated with a poor prognosis. TAMs interact with infiltrating lymphocytes and may supply immunosuppressive signals to attenuate antitumour T-cell activity	Nanoparticles with high affinity for TAMs	Dextran-coated cross-linked iron oxide (CLIO) magnetofluorescent nanoparticles: AMTA680 (shown to selectively label endogenous TAMs)		T_2-weighted RARE sequence MRI was performed at 7 T both before and 24 h after injection of AMTA680 in a murine soft-tissue sarcoma model. MRI identified submillimetre foci of hypointense signal generated by the AMTA680-labelled TAMs. Depletion of the endogenous TAM population caused by anti-TAM therapy was demonstrated by fluorescence molecular tomography but not MRI. This work demonstrates that MRI successfully detects AMTA690-labelled TAMS, allowing *in vivo* tracking and localisation with the potential to diagnose tumour progression and follow response to therapy	(57)

BOA, bis-oleate; ECM, extracellular matrix; GdDOTA, gadolinium-tetraazacyclododecanetetraacetic acid; GdDTPA, gadopentate dimeglumine; GDP, guanosine diphosphate; GTP, guanosine triphosphate; mAb, monoclonal antibody; MGRE, multi-gradient echo; RARE, rapid acquisition with relaxation enhancement; SPIO, superparamagnetic iron oxide; TGF, transforming growth factor.

be further enhanced (27). Importantly, the relatively low sensitivity of detection of MRI compared with either single photon emission computed tomography (SPECT) or positron emission tomography (PET) means that, in order to be sufficiently effective, MRI probes must either be multivalent, e.g. consisting of multiple chelated Gd^{3+} ions, or be limited to the detection of high-density epitopes ($\geq 10^6$ receptors per cell) (28). These limitations have necessitated the development of amplification strategies in order to improve SNR, in addition to targeting the probe successfully.

Initial attempts to target molecules/receptors of the TME employed gadolinium-conjugated monoclonal antibodies (mAbs). However, mAbs have undesirable pharmacokinetic properties, such as long blood plasma circulation times, large size and requisite high protein doses. These properties hinder solid tumour penetration, meaning that mAbs are better suited for the detection of vascular rather than tumour cell-specific targets. Furthermore, nontarget biodistribution of mAbs is substantial, with uptake apparent in the liver and spleen. Finally, in spite of the high target receptor specificity and affinity exhibited by mAbs, optimal contrast can take 24–48 h to manifest, which complicates clinical application (29). The direct conjugation of gadolinium chelates to targeting moieties represents another method by which the specificity of targeting can be ensured, and an application to the TME has been reported (30). We continue by discussing those aspects of the TME that have been evaluated using the various means described of generating MR-based contrast.

VASCULATURE

To satisfy its requirement for a sufficient supply of nutrients and oxygen, the tumour develops its own blood vascular network, and tumour vasculature is probably the most intensively investigated aspect of the TME (Fig. 2). Most tumour vascular networks are structurally and functionally abnormal, and, in
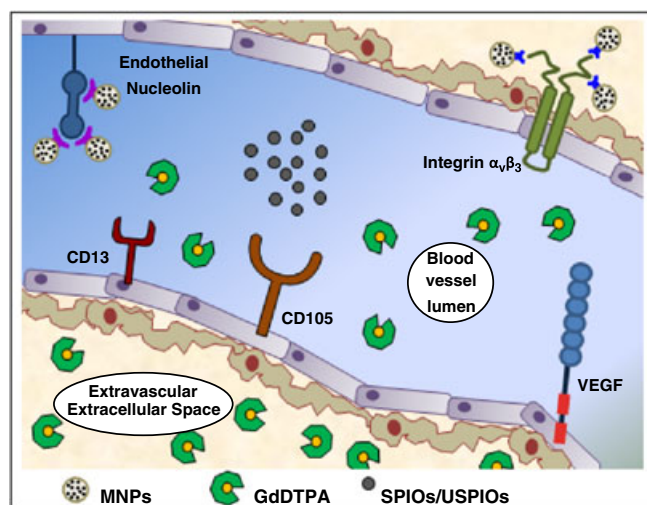

Figure 2. Tumour vasculature. Numerous tumour vascular markers have been imaged by active targeting of antibodies and peptides coupled to contrast moieties. Tumour perfusion can be pharmacokinetically modelled using dynamic contrast-enhanced MRI (DCE-MRI) data. GdDTPA, gadopentate dimeglumine; MNP, magnetic nanoparticle; SPIO, superparamagnetic iron oxide; USPIO, ultrasmall superparamagnetic iron oxide; VEGF, vascular endothelial growth factor.

particular, their perfusion and permeability characteristics differ from those of non-neoplastic tissues (31).

A number of techniques have been used to evaluate the vasculature and response to vascular disrupting agents (VDAs) and antiangiogenics. These include DCE-MRI and less commonly used methods, such as susceptibility contrast MRI, vessel size index and a combination of dynamic susceptibility-weighted perfusion MRI and dynamic gadolinium-enhanced MRI. By using probes specifically targeted to markers of angiogenesis and aspects of the vasculature, such as integrins and cell surface nucleolins, MRI can provide more information on the underlying physiological processes.

DCE-MRI has proven to be an invaluable tool in the noninvasive assessment of tumour microvasculature characteristics, and is already a mainstream diagnostic modality for many tumour types in radiological practice (31). DCE-MRI can differentiate between benign and malignant neoplasms on the basis of their respective microcirculations (16). The tumour vasculature is a key therapeutic target and DCE-MRI has had considerable success in clinical trials by providing imaging biomarkers for the effectiveness of many antiangiogenic drugs and VDAs (17). For example, DCE-MRI has been used to monitor the effects of a tyrosine kinase inhibitor targeted to vascular endothelial growth factor (VEGF). The effect of PTK787/ZK222584 (PTK/ZK) was observed in patients with advanced colorectal carcinoma (32). In this study, a significant negative correlation between the percentage baseline bidirectional transfer constant (K_i) and the increase in PTK/ZK oral dose and plasma levels was observed. The authors suggested that the methodology could be applied to define the pharmacological response and dose of antiangiogenic therapies, such as PTK/ZK. Galbraith et al. (33) used DCE-MRI to investigate the antivascular effect of the VDA combretastatin A4 phosphate (CA4P) on human and rat tumours in vivo by monitoring the tumour transfer constant K^{trans}. Another VDA, ZD6126, disrupts the tubulin cytoskeleton of proliferating neo-endothelial cells, resulting in tumour blood vessel destruction and congestion and haemorrhagic necrosis (34). DCE-MRI and multi-gradient echo (MGRE) have been used to study ZD6126-treated rat GH3 prolactinomas and RIF1 fibrosarcomas. Robinson et al. (34) demonstrated that ZD6126 (50 mg/kg) treatment reduced the initial area under the concentration–time curve (IAUC) to zero across the majority of the tumour, and a further example of this dramatic effect is depicted in Fig. 3. A decrease in R_2* observed 24 h post-treatment was explained by the agglomeration of erythrocytes in small focal areas. The changes in DCE-MRI endpoints were attributed to a dose-dependent induction of massive core tumour necrosis, which was confirmed histologically. A continuation of this work later confirmed that IAUC, and hence tumour perfusion, does not recover, even at 96 h post-treatment (35). ZD6126 has also been evaluated in a prostate cancer xenograft model using diffusion and vascular imaging. This study reported a significantly lower tumour vascular volume 24 h after therapy. Diffusion changes in the tumour were evident at 48 h and also correlated with necrosis (36). ZD6126 has undergone phase I and II clinical trial testing: Phase I studies showed antivascular effects on DCE-MRI, but there were dose-limiting cardiac side-effects (37). Two phase II trials in metastatic colorectal and renal cancer were stopped because of cardiac toxicity (38).

Recently, alternative MRI methods, including susceptibility contrast MRI and vessel size index MRI, have been used for the assessment of rat tumour response to various antivascular treatments (39–41). Using vessel size index MRI, Howe et al. (41)
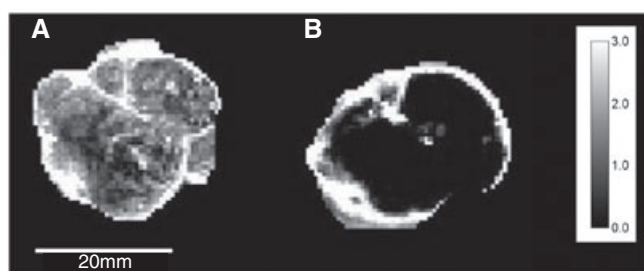
Figure 3. Dynamic contrast-enhanced MRI (DCE-MRI) detects tumour response to the vascular disrupting agent, ZD6126. Representative quantitative maps of IAUC60 (IAUC, initial area under the concentration–time curve) for gadopentate dimeglumine (GdDTPA) of a rat GH3 prolactinoma before (A) and 24 h after (B) treatment with ZD6126 (50 mg/kg). Note the dramatic reduction in IAUC60 in the core of the tumour, resulting from the reduction in blood flow in response to the agent. These data were normalised to the median muscle value to reduce the effect of variations in arterial input function between scans. The scale bar therefore represents 0–3 times the median muscle value in this particular rat. Figure courtesy of Dr D. J. O. McIntyre and Dr S. P. Robinson (unpublished data).

monitored the effect of the VDA 5,6-dimethylxanthenone 4-acetic acid (DMXAA) on the estimated fractional blood volume (fBV) in rat GH3 prolactinoma xenografts. To determine fBV and the vessel size index (R_v), an ultrasmall superparamagnetic iron oxide particle (USPIO) (Ferumoxtran-10) challenge was administered, which induced large susceptibility changes by increasing R_2^*, detected by MGRE. USPIOs remain in the vessel, unlike gadopentate dimeglumine (GdDTPA), and therefore measure vessel size but not permeability. The changes observed in fBV and R_v imaging biomarkers were consistent with the known mode of action of DMXAA. The response of rat GH3 prolactinoma xenografts to ZD6126 has also been measured by susceptibility contrast MRI (39). This study made use of an alternative USPIO (Feruglose) and demonstrated a highly significant reduction in tumour fBV at 24 h post-treatment. Here, the authors suggested that, compared with DCE-MRI, susceptibility contrast MRI may provide a more robust approach for assessing the individual effects in combination therapies designed to eliminate the viable tumour rim and enhance the activity of ZD6126 (39). Using intrinsic susceptibility, McPhail et al. (40) studied the effects of DMXAA and CA4P on rat GH3 prolactinomas, without the need for USPIO administration. Changes in R_2^* were detected as an imaging biomarker of tumour vascular response to VDA therapy. A significant decrease in R_2^* was observed in CA4P-treated tumours alone and was attributed to reduced tumour blood volume caused by prolonged CA4P-induced vascular collapse. These results indicated that CA4P was more effective than DMXAA in this rat tumour model.

A combination of dynamic susceptibility-weighted perfusion MRI, using the USPIO Ferumoxytol (providing T_2^*-weighted data), and dynamic gadodiamide-enhanced MRI (providing T_1-weighted data) to assess vascular permeability has recently shown promise for the accurate detection of the therapeutic response to antiangiogenic therapy in a U87 human glioma xenograft model. Varallyay et al. (42) reported that, following a single dose of bevacizumab, a statistically significant decrease in relative cerebral blood volume (determined using the USPIO Ferumoxytol) was observed up to 72 h post-contrast. In addition, the time-to-peak, determined by gadodiamide-enhanced MRI, demonstrated a statistically significant decrease at 48 and 72 h post-contrast. Changes in both relative cerebral blood volume and time-to-peak

were normalised and compared with untreated controls. This study enabled the simultaneous *in vivo* assessment of U87 glioma xenograft perfusion and permeability in response to antiangiogenic bevacizumab therapy. However, the mechanisms underlying the observed physiological responses are not yet fully understood. The authors emphasise the need to identify specific biomarkers when enhancement alone is clearly insufficient in the accurate assessment of response.

Although DCE-MRI kinetic parameters have long been used as markers of response to antiangiogenic agents and VDAs, they do not shed light on the physiological mechanisms underlying the response. This is an area in which specifically targeted MRI probes show potential utility. A number of markers of angiogenesis have now been targeted, including VEGF, integrins and cell surface nucleolin.

A study by Reddy et al. (43) demonstrated the efficacy and versatility of multifunctional MNPs for targeting photodynamic therapy (PDT) to brain tumours *in vivo*. PDT makes use of photosensitising drugs which, when excited, react with molecular oxygen *in situ* to generate cytotoxic reactive oxygen species and cause tissue necrosis. Multifunctional MNPs consisting of encapsulated iron oxide and Photofrin, a sensitiser required for effective photo-irradiation, were conjugated to the F3 peptide which binds to nucleolin on tumour angiogenic endothelium, allowing the targeting of therapy. In a 9L glioma xenograft model, MRI was used to demonstrate the uptake and distribution of multifunctional MNPs. Treatment with PDT led to increased survival compared with nontargeted PDT.

Integrins are cell adhesion molecules; within the TME, they are expressed on endothelial cells and tumour cells. By mediating movement and invasion, they play key roles in metastasis and angiogenesis; they are also involved in cross-talk with growth factor receptors (44). Integrin $\alpha_v\beta_3$, the most studied by MRI, binds to the RGD (arginine–glycine–aspartic acid) tripeptide sequence present on proteins such as fibronectin. Integrin $\alpha_v\beta_3$ expression is up-regulated in both tumour cells and angiogenic endothelial cells. Imaging of $\alpha_v\beta_3$ has been performed with MNPs (45) allowing the noninvasive detection of levels of angiogenesis *in vivo* (46–50) (Table 2). The quantification of $\alpha_v\beta_3$ expression could potentially be used to monitor the treatment response to antiangiogenics, or even in the selection of patients most likely to respond to treatment with antiangiogenics; however, as yet, there are no studies reporting on tumour response to therapy. Other vascular targets for MRI include CD105 (expressed on immature tumour vessels) (51) and CD13 (expressed on activated endothelial cells) (52): these are summarised in Table 2.

TARGETING OF IMMUNE CELLS

Motile, infiltrating immune cells are a key feature in the ECM and have an important role to play in the potential treatment of tumours. Cellular therapies using stem cells or immune cells are increasingly being applied in clinical trials, although immune responses are evoked only in a minority of patients, possibly because of the ineffective delivery of cells to target organs (53). MRI can be used to track immune cells that have been labelled with MNPs (Fig. 4). MNP-labelled natural killer (NK) cells targeted against the Her-2/neu receptor have been shown to accumulate in a mouse mammary NIH 3T3 xenograft, as summarised in Table 2 (54).

Tumour antigen-loaded dendritic cell (DC) therapy enhances the immune response raised against the tumour, and is currently an
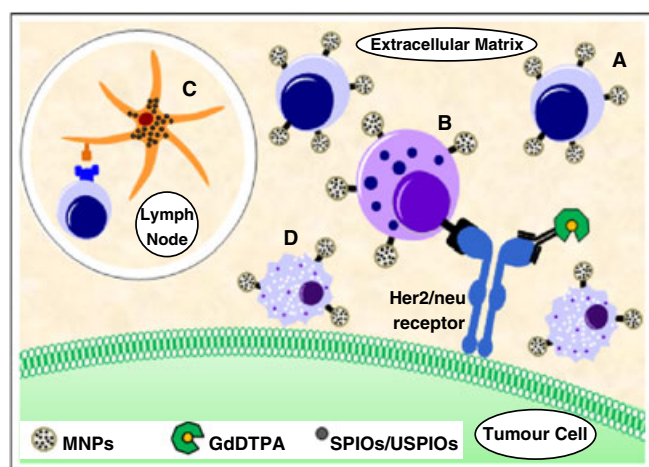
Figure 4. Imaging immune cells. MRI has been used to track immune cells in the tumour microenvironment by labelling motile immune cells with various contrast moieties: (A) Magnetic nanoparticle (MNP)-labelled T-lymphocytes; (B) MNP-loaded natural killer (NK) cells targeted to the Her2/neu receptor; (C) dendritic cells (DCs) engulf superparamagnetic iron oxide (SPIO) particles and present antigen to immature cells in the lymph nodes (inset); (D) AMTA680-labelled tumour-associated macrophages (TAMs). GdDTPA, gadopentate dimeglumine.

accepted treatment option for melanoma. DCs engulf SPIOs as part of their normal physiological phagocytic function (Fig. 4). de Vries *et al.* (53) have been able to track *in vitro*-generated, SPIO-labelled DCs loaded with tumour-derived antigenic peptides administered to stage III melanoma patients via intranodal injection. The authors recommended their approach for extended clinical applications, such as the monitoring of monocyte, granulocyte and lymphocyte trafficking. Tumour infiltration by intraperitoneally injected iron oxide-labelled T-cells has also been observed preclinically *in vivo* and correlated with response. In a study by Hu *et al.* (55), T_2-weighted MRI demonstrated that activated MNP-labelled T-cells accumulated in tumours undergoing immune rejection/regression. Sengar *et al.* (56) have also demonstrated the feasibility of monitoring DC delivery, trafficking and localisation *in vivo* in 9L glioma rat brain xenografts.

Tumour-associated macrophages (TAMs) are bone marrow-derived mononuclear phagocytes that are recruited by tumours. Within the TME, they participate in tumour invasion, angiogenesis and metastasis formation, and can modulate tumour-specific T-cell immunity. An accumulation of TAMs is associated with a poor prognosis, whereas the removal of TAMs has been shown to lead to tumour regression in animal models (57). Studies by Valable *et al.* (58) and Leimgruber *et al.* (57) have demonstrated the feasibility of *in vivo* MRI tracking of macrophages labelled with micrometre-sized fluorescent particles of iron oxide and MNPs, respectively. Leimgruber *et al.* (57) made use of dextran-coated MNPs (AMTA680) with an ability to selectively label TAMs *in vivo*. The *in vivo* distribution of AMTA680-labelled TAMs was studied using MRI in a mouse soft-tissue sarcoma model. Submillimetre foci of hypointensity on T_2*-weighted images (generated by the SPIO core of AMTA680) were observed 24 h after the administration of AMTA680-labelled TAMs. Fluorescence molecular tomography, but not MRI, was used to quantitatively assess changes in TAM populations in response to anti-TAM therapy (pro-apoptotic clodronate-loaded liposomes). This demonstration of molecular imaging multiplexing has clinical

potential for the monitoring of tumour progression, and for the assessment of the efficacy of cellular-based cancer therapies.

MEASUREMENT OF TME METABOLITES

MRS can be used both to detect and quantify a number of metabolites, and also to measure the pH and energy status of tumours; spatial images of the metabolite concentrations within the TME can be produced using MRSI. Many studies have evaluated the MR spectra of tumours relative to those of normal tissue, as well as the MRS changes in response to chemotherapy, radiotherapy and molecularly targeted therapies; there are several excellent recent reviews of this area (59,60). ^{1}H MRS, the most widely used method, provides the highest sensitivity of detection, allowing the spatial distribution of metabolites within a tumour (e.g. choline, creatine, myo-inositol or lactate) to be imaged by MRSI.

In the present context, it is important to recognise that the metabolite signals detected by MRS will include contributions from the tumour cells, the cellular component of the TME and the TME's extracellular compartment. In MRS evaluation of prostate cancer, for instance, extracellular citrate is an important factor, as it is present in normal prostate and reduced or absent in prostate cancer (61). A number of studies have shown that prostate tumours have increased ratios of choline (mainly in the tumour cells) to citrate (mainly in the extracellular TME) (62). The decrease in citrate seen in malignancy is possibly a result of changes in cellular function and a loss of ductal morphology, with the replacement of glands by tumour cells leading to reduced luminal space and therefore reduced citrate (63). Most studies have concentrated on the diagnosis and grading of prostate cancer; however in response to hormone therapy, loss of citrate correlated roughly with decreasing serum prostatic specific antigen levels (64). ^{1}H MRS has also been used to evaluate the extracellular compartment of the brain. A trial of single-voxel MRS of peritumoral oedema was performed in 23 patients with various brain tumours (gliomas, metastases and meningiomas) (65). Glutamate levels in peritumoral oedema were significantly elevated in tumours of nonglial origin compared with glial tumours or normal white matter. This was thought to be a result of the expansion of the extracellular space caused by oedema. Many anticancer treatments are pro-apoptotic. During apoptosis, there is an accumulation of cytoplasmic lipid vesicles which are detectable by ^{1}H MRS. Changes in tumour lipid in response to therapy have also been monitored by ^{1}H MRS in lymphoma and glioma models (66,67).

^{19}F MRS can also be used to investigate the effect of the TME on the uptake of the fluorinated drug 5-fluorouracil (5-FU), as the active drug species – phosphorylated anabolites – are only formed intracellularly. A study by Gade *et al.* (68) used ^{31}P/^{19}F MRS to evaluate tumour bioenergetics and the delivery of 5-FU to subcutaneous tumours in mice that had been treated with type I collagenase to degrade collagen, a major constituent of the tumour matrix. In mice treated with collagenase, the tumour interstitial fluid pressure (IFP) was reduced significantly compared with controls, but the tumour blood flow was unaltered. ^{19}F MRS-measured levels of 5-FU were found to be, on average, 1.5 times higher in mice treated with collagenase than in untreated mice. However, this did not result in higher levels of the anabolite fluoronucleotides that are required for 5-FU cytotoxicity, and there was no significant difference in tumour growth rates between mice treated with collagenase + 5-FU and controls.

MEASUREMENT OF TME pH

The TME is frequently characterised by an acidic extracellular pH (pH_e), with typical values in the range pH 6.3–6.99 (11); it can be detected by MRS of an extracellular probe, such as 3-aminopropylphosphonate, which allows the simultaneous measurement of pH_e and the intracellular pH (pH_i) by ^{31}P MRS (69). To improve spatial resolution, pH-sensitive spectroscopic imaging probes have been developed for use with ^{1}H or ^{19}F MRSI (70,71). For example, imidazol-1-yl-3-ethoxycarbonylproprionic acid (IEPA) and 2-imidazol-1-yl succinic acid (ISUCA) have been used in conjunction with ^{1}H MRSI to generate localised pH_e maps of tumours in mice and rats, with a resolution approaching 1 mm^3 (72,74).

In the last decade, pH-sensitive gadolinium chelate contrast agents have been developed to generate pH_e maps in tumours with ^{1}H MRI resolution (75,76). However, this MRI T_1 relaxometry technique requires correction for the concentration of the contrast agent in each image pixel, necessitating the administration of a second pH-insensitive contrast agent with a similar pharmacokinetic profile to the pH-sensitive contrast agent, which, in practice, is very difficult to achieve *in vivo* (77). However, very recently, the development of a pH-sensitive bimodal MR PET agent has enabled the direct determination of pH_e-dependent T_1 relaxation by MRI and the concentration of the agent itself by PET (78). A number of researchers have used MRI techniques, such as amide proton transfer (APT) and chemical exchange saturation transfer (CEST) imaging, to determine pH in solutions and *in vivo* (79–81).

There would be many potential clinical applications of pH imaging should the many barriers to translation, particularly the potential toxicity of pH imaging agents (82), be overcome. In addition, the inherently low sensitivity of MRS makes it difficult to obtain high-resolution pH_e maps without a prohibitively long acquisition time (83), and the detection of the relatively small pH-dependent chemical shift exhibited by these agents and accurate estimation of pH_e may not be feasible at clinically relevant field strengths. However, recent work using nontoxic hyperpolarised ^{13}C-bicarbonate to generate pH_e maps of the TME by ^{13}C MRSI in an experimental tumour model offers hope of a pH_e imaging technique that could be translated into the clinic (82). The dramatically higher sensitivity of hyperpolarised ^{13}C MRSI also affords a significant reduction in acquisition time.

In the context of monitoring the TME response to therapeutic intervention, perhaps the most exciting use of pH_e imaging lies in its potential to assess the efficacy of drugs targeting tumour metabolism. Imaging pH_e offers an attractive way to monitor the efficacy of this class of drug, because the end-products of central carbon metabolism are invariably acids, e.g. lactate and carbonic acids (84). Such drugs are predicted to affect pH_e to a greater extent than pH_i because tumour cells adopt mechanisms to maintain a relatively constant pH_i, whereas the extracellular space in tumours is poorly buffered (85), and H$^+$ ions are inefficiently cleared by the typically abnormal tumour vascular network (86). Noninvasive monitoring of tumour pH_e by MR therefore offers an attractive means of determining the efficacy of these drugs in preclinical and clinical development.

The measurement of the pH_e of the TME also has potential value in predicting the likelihood of conventional cytotoxic drugs gaining entry to the cancer cell, and therefore the potential benefit of the treatment. Drug delivery into the cancer cell is affected not only by tumour perfusion and the stromal compartment, but also by pH_i and pH_e (87). The antitumour activities of several weakly ionising chemotherapeutic drugs have been shown to be affected by the action of the transmembrane pH gradient on the distribution of charged and uncharged species of the drug in the intra- and extracellular spaces (the 'ion trapping' phenomenon) (88). As a consequence of the acidic pH_e, weakly basic chemotherapeutic drugs, such as doxorubicin, mitoxantrone, vincristine and vinblastine (with acid dissociation constants pK_a of 7.5–9.5), are protonated and become trapped in the extracellular space (89). This physiological drug resistance has been demonstrated to reduce the cellular uptake of such weakly basic compounds *in vitro* (90) and *in vivo* (91), and has led to attempts to improve drug delivery by alkalinising the extracellular space with bicarbonate (91). Conversely, low pH_e has been shown to promote the entry of weakly acidic drugs, such as chlorambucil and cyclophosphamide, into the cell (92). Imaging of pH_e and the measurement of pH_i by ^{31}P MRS permit the estimation of the transmembrane pH gradient, which can then be used to predict which class of drug is more effectively delivered into the cell. This information could aid in the selection of patients with tumours that have steep transmembrane pH gradients, for whom one would tailor chemotherapy to avoid the use of weakly basic drugs in favour of weakly acidic drugs.

MEASUREMENT OF TME TEMPERATURE

In normal tissues, heat induces a prompt increase in blood flow, accompanied by dilation of vessels and an increase in permeability of the vascular wall (93). Compared with normal tissues, the capacity of tumour blood flow to increase on heating is limited. The tumour vasculature is therefore less able to dissipate heat and more likely to be damaged when treated with hyperthermia. Consequently, tumours tend to develop higher temperatures than surrounding normal tissues during heating, and thus greater heat damage occurs within tumours (93). In tumours, increased blood flow and decreased oxygen demand ultimately result in an increase in tumour tissue oxygenation. Hyperthermia may therefore represent the best hypoxic radiosensitiser available (94).

Various MR-based methods of determining tissue temperature *in vivo* have been described and concisely reviewed (95). Peller *et al.* (96) have demonstrated that relative changes in T_1 are linearly correlated with temperature over a range of hyperthermia-relevant temperatures (32–44 °C) in amelanotic melanoma A-MEL-3 xenografts, and that T_1 allows the *in vivo* assessment of both temperature changes and tissue changes at low and high thermal doses, respectively. MR thermometry alongside ablative therapy is also being implemented in the clinic. In 2003, Dick *et al.* (97) demonstrated that MR-guided laser thermal ablation (LTA) of hepatic tumours is feasible, safe and efficacious, reducing viable hepatic tumour tissue by 50.7% after 4–6 weeks. Colourised T_1-weighted thermal maps generated in near real time exhibited moderate correlation with follow-up gadolinium-enhanced MRI and were useful in predicting the ablated area (97). Martin (98) described interventional MRI (iMRI) as the current standard of care in estimating hepatic tumour thermometry during ablative therapy, although this review focused on ablative techniques in general rather than the specific iMRI methods; it also emphasised the need for

continued evaluation of iMRI to establish common guidelines for all patients undergoing hepatic tumour ablation. Gellerman et al. (99) have employed the proton resonance frequency shift method to demonstrate the feasibility of using noninvasive MR thermometry to monitor tumour temperature changes during regional hyperthermia in nine patients with high-risk soft-tissue sarcomas. In an ongoing feasibility study using the same methodology, Siddiqui et al. (100) have shown that it is possible to use MRI-guided high-intensity ultrasound therapy to accurately target localised prostate tumours in patients.

MEASUREMENT OF TME OXYGENATION

It is widely acknowledged that tumour cell hypoxia influences the treatment and progression of cancer. Molecular oxygen is required for the fixation of radiation damage to DNA, so that high metabolic consumption as well as the compromise of oxygen delivery by inadequate perfusion result in resistance to radiotherapy. The poor vascular perfusion of tumours, which is responsible for hypoxia (Fig. 5), also impairs drug delivery, thus reducing the efficacy of chemotherapy (11). Although there is increasing interest in the feasibility of imaging hypoxia *in vivo*, there is currently no gold standard available for the assessment of tumour hypoxia in patients. The development of a noninvasive MR-based means of assessing tumour oxygenation *in vivo* would have important implications for the effective treatment of cancer; enabling radiologists to both detect and evaluate tumour oxygenation prior to radiation therapy, and also to monitor response to tumour oxygenating agents, which may be administered in an attempt to overcome radiation resistance (101,102). We review a number of direct and indirect MR-based techniques being applied to the *in vivo* evaluation of TME oxygenation.

In 2000, Cooper et al. (103) investigated the relationship between tumour oxygenation and DCE-MRI parameters in an attempt to identify a noninvasive technique for the *in vivo* detection of tumour oxygenation. DCE-MRI data were acquired

Figure 5. Tumour microenvironment: physical effects. Tumour partial oxygen pressure, pH, water content/mobility and temperature are factors that influence the functionality of the tumour microenvironment, all of which can be probed using various MR techniques.

for a series of patients with locally advanced carcinoma of the cervix, pre- and post-external beam radiotherapy. The time–intensity curve was used to calculate the increase in SI over baseline, which had previously been shown to correlate closely with pharmacokinetic parameters. DCE-MRI data were compared with tumour oxygenation levels determined by polarographic needle electrode measurements, and a significant correlation between tumour oxygenation and the increase in SI was observed. However, correlations between DCE-MRI and the partial oxygen pressure (p_{O_2}) are inevitably indirect because DCE-MRI provides estimates of tumour vascular flow, volume and permeability, rather than tumour hypoxia or oxygen delivery and consumption (104,105).

Blood oxygen level-dependent (BOLD) MRI is an alternative means of measuring oxygenation of the TME, although it is not possible to measure absolute p_{O_2} by this method. Instead, BOLD contrast is generated by a period of intervention, e.g. breathing hyperoxic gas, which alters the ratio of deoxygenated and oxygenated haemoglobin species in the blood, modulating tissue R_2^*. This permits the detection of relative changes in paramagnetic deoxyhaemoglobin concentration and blood flow in tumours, using T_2^*-sensitive sequences such as gradient recalled echo (11). Since the first example of BOLD changes in contrast in 1990, several studies in tumour models have indicated a correlation with relative p_{O_2} (106–109). Differing BOLD contrast has been used widely as an *in vivo* marker of changing tumour oxygenation (110,111).

Griffiths et al. (112) used BOLD to study the response of tumours in patients to breathing carbogen. Half of the tumours studied demonstrated enhanced SI following carbogen breathing, consistent with improved tumour oxygenation and blood flow. A lack of enhancement was postulated to be a result of poor perfusion, necrosis, hypoxic tissue (which did not respond to carbogen) or fully oxygenated tissue. There was evidence of heterogeneity of response, even within a single tumour, and also of 'steal' phenomena, where vasodilation in one region of the tumour steals the blood from another region. However, quantification of the BOLD effect in response to carbogen is complicated because changes in SI are affected not only by tissue p_{O_2}, but also by tissue pH, haematocrit and flow (11). In addition, breathing carbogen is uncomfortable for the patient.

BOLD has also been evaluated for the real-time observation of antivascular PDT in solid M2R mouse melanoma xenografts (113). Gross et al. (113) investigated whether antivascular PDT-induced photoconsumption of oxygen and the consequent haemodynamic effects could be detected by a change in BOLD contrast. This study reported on a new family of photosensitising agents with superior properties to those in use in the clinic at that time. The lead compound, TOOKAD-PDT, started clinical trials in 2002 for the treatment of prostate cancer. Following TOOKAD-PDT administration, a rapid decrease in BOLD contrast was observed solely in the tumour region of interest. The greatest effect was seen at the tumour rim, which was in agreement with the spatial distribution of PDT-induced lipid peroxidation. These results suggested that a rapid, local, photosensitised MR BOLD contrast was generated during PDT, and that photosensitised BOLD MRI may provide the means for real-time guidance and assessment of PDT.

Using a combination of DCE-MRI and BOLD-MRI, Zhao et al. (114) assessed R3327-AT1 rat prostate tumour response to continuous low-dose metronomic chemotherapy (M-CTX) alone, or in combination with antiangiogenic thalidomide. Tumour
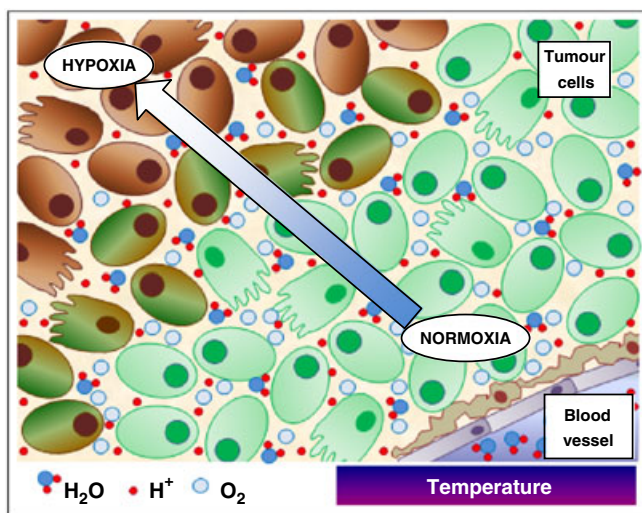
perfusion was evaluated on the basis of the area under the signal intensity–time curve (AUC) generated using DCE-MRI. A shift to the left of the AUC histograms was observed with time for all tumours, although the effect was more pronounced in treated tumours. Significant changes in AUC were observed for the centre of treated tumours by day 3, compared with baseline and control tumours. However, R_2* values did not correlate with growth in the control group or in the M-CTX or M-CTX + thalidomide therapy groups. Alonzi *et al.* (115) later quantified the BOLD effect by the calculation of R_2* values, and demonstrated that breathing carbogen increases prostate tumour oxygenation in PC3 and DU145 xenografts.

O'Connor *et al.* (105) described the application of a method distinct from BOLD, termed oxygen-enhanced imaging. Three-dimensional T_1-weighted MR images were acquired whilst patients with advanced cancer of the abdomen or pelvis underwent a period of breathing 100% oxygen, sandwiched between periods of breathing medical air (21% oxygen). Serial oxygen-enhanced MR images were used to calculate tumour R_1 values through time. Oxygen-induced MRI ΔR_1 values were compared with the spatial distribution of perfusion, as determined by DCE-MRI. A statistically significant oxygen-induced ΔR_1 was demonstrated in eight patients and found to be independent of tumour mean basal R_1 and tumour size. Temporal evolution of ΔR_1 was observed when the patients switched from breathing medical air to 100% oxygen. This preliminary study claims to provide the first clinical evidence that oxygen-enhanced MRI is feasible and well tolerated by patients, and recommends further investigation into the use of this method as a noninvasive technique of mapping changes in tumour oxygen concentration. However, it may be that the results presented in this study were confounded by hyperoxia-induced vasoconstriction, as discussed by Gillies *et al.* (11): breathing carbogen during the intervention period is generally preferred to breathing oxygen, as the hypercapnia induced by carbogen is believed to block hyperoxic vasoconstriction.

Mason *et al.* (101) have proposed that, to fully characterise tumour hypoxia noninvasively, a combination of assessment of T_1- and T_2-weighted changes induced by breathing hyperoxic gases is needed. A technique such as dynamic oxygen challenge evaluated by NMR T_1 and T_2* (DOCENT) would exploit both BOLD and tissue oxygen level-dependent (TOLD) contrast in order to achieve a robust prognostic clinical test to reveal tumour hypoxia.

Tumour hypoxia has also been evaluated *in vivo* by the direct measurement of TME p_{O_2} using MR-based methods, such as Overhauser-enhanced MRI (OMRI), ^{19}F NMR spectroscopy, electron paramagnetic resonance (EPR) oximetry, ^{1}H MRS and ^{19}F MRI (116,117).

^{19}F MRI and MRS of perfluorocarbons (PFCs) and fluorinated nitroimidazoles have been used extensively to detect tumour hypoxia *in vivo*. The ^{19}F spin–lattice relaxation rates of PFCs vary linearly with increasing oxygen tension *in vivo*. The high solubility of oxygen in PFC emulsions, coupled with the ability to overlay ^{19}F MRI images on conventional ^{1}H MRI images, means that a highly sensitive measure of tissue oxygen tension can be obtained and accurate tumour p_{O_2} maps can be generated. Nitroimidazole compounds undergo bioreductive metabolism in hypoxia and bind to tissue macromolecules. Various fluorinated nitroimidazoles used for the detection of hypoxia by ^{19}F MRS/MRI (118–122) are discussed below.

Of the PFCs, perfluoro-15-crown-5-ether (15C5) and hexafluorobenzene are considered to be the best, as they contain 20 and six magnetically equivalent fluorine atoms, respectively, thus increasing the signal to noise of their ^{19}F spectra. They are minimally sensitive to temperature changes and give a spectrum containing a single narrow peak, resulting in no chemical shift artefact problems, straightforward mapping of PFC T_1 and hence the local oxygen concentration (123). ^{19}F MRI has successfully predicted that a combination of 15C5 and carbogen can increase the radiosensitivity of subcutaneous rhabdomyosarcomas (102). However, one of the limitations of PFCs is that invasive microelectrodes (such as directly implanted PFC droplets) usually give much lower tumour p_{O_2} measurements than *in vivo* MR measurements acquired following the intravenous administration of PFCs, probably because intravenous PFC is sequestered in a well-oxygenated region close to the tumour blood vessels (124,125). To combat the problems associated with the intravenous administration of PFC emulsion, or direct intratumoral injection of PFC droplets, Noth *et al.* (126) subcutaneously co-administered 15C5-loaded oxygen-permeable alginate capsules together with tumour homogenate (GH3 prolactinoma) in the flanks of Wistar Furth rats in order to monitor changes in the TME p_{O_2} by ^{19}F MRI during 26 days of tumour growth, as well as the p_{O_2} response to various modifiers, including carbogen. An initial increase in tumour p_{O_2} was observed, probably indicating the onset of neovascularisation (the 'angiogenic switch'), followed by a decrease after week 2, probably indicative of the development of hypoxia/necrosis as the tumour outgrew its blood supply. Breathing carbogen increased tumour p_{O_2}. The high sensitivity of hexafluorobenzene as an indicator of tumour oxygenation has also been demonstrated using ^{19}F MRS (127).

Kodibagkar *et al.* (117) have described a novel ^{1}H probe of p_{O_2}, named hexamethyldisiloxane, which exhibits high sensitivity to changing p_{O_2}, little response to temperature and a single ^{1}H resonance. This proof-of-concept study demonstrated the feasibility of using a ^{1}H probe for tumour hypoxia which could be implemented on clinical scanners lacking ^{19}F capability.

In 2004, Zhao *et al.* (128) reviewed methods for the measurement of tumour oxygenation *in vivo* [for a summary, see table 1 of ref. (128)]. They described a novel procedure, known as fluorocarbon relaxometry using echo planar imaging for dynamic oxygen mapping (FREDOM). This technique takes tumour heterogeneity and fluctuations in intratumoral p_{O_2} into consideration and, as a result of the speed of imaging, allows repeated quantitative maps of regional p_{O_2} to be obtained simultaneously at multiple individual locations. In 2007, Bourke *et al.* (129) investigated the potential of FREDOM for predicting the response to radiation therapy in hypoxic Dunning prostate R3327-AT1 tumours grown in Copenhagen rats. Using FREDOM, large AT1 tumours were shown to have a significantly greater hypoxic fraction and lower mean p_{O_2} than smaller tumours. The mean p_{O_2} in large tumours responded to hyperoxic gas breathing, but the hypoxic fraction resisted modulation, rendering the tumours resistant to radiotherapy. Better oxygenated tumours showed better response to irradiation, and a correlation between time to double in volume and pretreatment p_{O_2} in individual tumours was shown. Together, these results demonstrated the prognostic value of imaging PFCs and strengthened the argument for the further development and application of FREDOM, and its application in the clinical evaluation of tumour oxygenation. Zhao *et al.* (109) went on to compare their FREDOM technique with ^{1}H BOLD MRI in the evaluation of tumour oxygenation in response to hyperoxic

(100% oxygen) gas challenge. ^{1}H BOLD MRI and ^{19}F NMR echo planar imaging FREDOM data were acquired as rats bearing mammary carcinoma xenografts breathed air (baseline) and then oxygen. For a group of nine tumours, a significant correlation was found between mean Δpo_2 and ΔSI detected by ^{19}F tumour tissue oximetry and ^{1}H BOLD MRI, respectively. The main drawback of FREDOM is the current lack of Food and Drug Administration (FDA) approval for the human use of PFCs, presenting a barrier to its clinical translation and validation (109).

Another approach to the detection of po_2 of the TME involves nitroimidazole compounds that react covalently with tissue components in hypoxic regions. Maxwell *et al.* (130) were the first to demonstrate tumour-selective retention of a monofluorinated nitroimidazole (Ro 07–0741) and a hexafluorinated misonidazole analogue (CCI-103F) *in vivo* using ^{19}F MRS. Later studies have focused on SR-4554, a fluorinated 2-nitroimidazole compound designed to act as a noninvasive probe of tumour hypoxia (131). SR-4554 has three magnetically equivalent ^{19}F atoms which remain detectable when the compound is covalently bound within a hypoxic cell. Extensive preclinical studies of SR-4554 have shown that the concentration of SR-4554 correlates well with po_2 values measured by polarographic electrodes (122,132–135). A phase I study of eight patients showed that SR-4554 was well tolerated, and that there was some evidence of ^{19}F retention in the three patients who underwent MRS (136). A further 26 patients have been evaluated in another phase I study, where higher doses were used and there was evidence of tumour retention of SR-4554 using ^{19}F MRS (137). As yet, these results have not been correlated with an alternative and accepted method of determination of tumour hypoxia. Another limitation is that the magnitude and rate of ^{19}F detection on localised MRS is low despite using high doses of SR-4554. As there is no room to increase the dose, alternative approaches would be to use higher field strengths or to increase the number of ^{19}F atoms on the nitroimidazole. Several other nitroimidazole hypoxia markers have been evaluated in the preclinical setting (138,139). TF MISO has been shown to be retained in a rat prostate tumour model (140). Both mTNF-1 and CF3PM were evaluated in a mouse model, and it was concluded that CF3PM could have potential for the evaluation of hypoxia by ^{19}F MRS (139). Although these markers have been detected, they have yet to be correlated with a response to therapy.

There are currently many barriers to the clinical translation of PFCs and fluorinated nitroimidazole compounds. As a result of the inherent insensitivity of MRI and MRS, the administration of high and (in the case of nitroimidazoles) potentially neurotoxic doses is required. High-molecular-weight PFCs, such as the 15C5 crown ether, tend to be sequestered permanently in the reticuloendothelial cells of the liver and spleen, whereas the lower molecular weight probes, such as PFOB, are excreted as vapour through the lungs. Further investigation into the clearance mechanisms of the probes is necessary. Until the benefit to the patient can be proven, in terms of prognostic value or evaluation of tumour response to therapy, the risks are currently considered to outweigh the benefits. The principles, applications and issues associated with the use of these probes have been comprehensively reviewed elsewhere (118,123).

EPR oximetry has demonstrated success in accurately assessing tumour po_2 *in vivo* in animals (141). Molecular oxygen is paramagnetic and affects the EPR spectra of a paramagnetic probe within its vicinity by altering the relaxation rate (and possibly other mechanisms) in a manner which is directly related to the amount of oxygen present (142). EPR oximetry therefore depends on the placement of oxygen-sensitive paramagnetic material within the tumour and, as such, is a minimally invasive technique (142). EPR oximetry represents a means of tracking changes in TME po_2, providing crucial information needed to optimise the effectiveness of hypoxia-modifying procedures and radiotherapy (142). Sentjurc *et al.* (141) successfully applied EPR oximetry to repeatedly measure po_2 of fibrosarcoma SA-1 xenografts prior to, during and following a course of therapy, and established that this methodology accurately reported on tumour blood flow changes induced by blood flow-modifying agents. Swartz *et al.* (143) discussed the feasibility of implementing EPR for the enhancement of tumour therapy, and reviewed the clinical studies currently underway. More recently, Khan *et al.* (144) have investigated the effect of carbogen inhalation and radiotherapy on tumour hypoxia in intracerebral orthotopic F98 glioma xenografts, and have reported that these tumours exhibit significantly lower po_2 compared with untreated contralateral normal brain tissue.

As with EPR oximetry, OMRI requires the administration of an exogenous paramagnetic agent to generate contrast. However, OMRI is a double-resonance technique which couples the advantages of MRI with the sensitivity of EPR (145). OMRI has demonstrated usefulness in the detection of tumour oxygenation in tumour-bearing mice (145). Thus far, the application of OMRI has been limited to the detection of variations in tumour po_2 and, to the authors' knowledge, it has not been used to evaluate changes in tumour vascular function or TME oxygenation in response to chemotherapy, radiotherapy or antiangiogenic treatment (146).

MEASUREMENT OF TME WATER MOBILITY AND PRESSURE

The IFP of normal tissue is actively regulated through interactions between stromal cells and the ECM (147). In tumours, dysregulated angiogenesis, combined with a lack of functioning lymphatic vessels and interstitial fibrosis, can result in elevated tumour IFP, which may represent a barrier against effective drug delivery (148). High IFP is characteristic of solid tumours of varying types, with values ranging between 10 and 100 mmHg (149), compared with normal values of between −1 and −3 mmHg (147). Historically, methods of measurement of IFP have been predominately invasive, with limitations akin to the aforementioned invasive methods of monitoring po_2. Recent advances in this field include the SAMBA-420 MR system, consisting of fibre-optic pressure transducers. This technology offers highly accurate absolute and relative pressure readings whilst being fully functional in the presence of a strong electromagnetic field (which may be of significance in the preclinical validation of MR methods for IFP measurement). However, the fragile tip of the SAMBA-420 MR renders it difficult to use in tissues with a hard consistency (148), which will limit its translational potential without further development of design. To date, a variety of MR applications have been trialled in the pursuit of a robust, repeatable, *in vivo*, noninvasive technique for the measurement of TME IFP.

Initial efforts by Lyng *et al.* (150) suggested that ^{1}H MRI T_1 and T_2 values could not be used clinically to assess tumour IFP and predict

the uptake of macromolecular therapeutic agents. Milosevic et al. (151) were the first to document the prognostic importance of pretreatment IFP measurement in a large prospective study of patients with cervical cancer, and to report that tumours with high IFP are more likely than those with low IFP to recur after radiotherapy and lead to death from progressive disease. IFP therefore represents another interesting imaging biomarker that could potentially be used to predict which tumours will respond to therapeutic intervention. Later work by Milosevic's laboratory demonstrated a negative correlation between the vascular permeability relative to muscle (rk_{trans}) and IFP in patients with cervical cancer (149). Although a negative correlation between rk_{trans} and IFP was deemed to be counterintuitive, it was reasoned that the permeability estimates in this study reflected blood flow resistance rather than vascular permeability. Hassid et al. (152) aimed to estimate the in vivo distribution of IFP in tumours using a new MRI application. Sequential MR images were acquired of human NCI-H460 nonsmall-cell lung cancer xenografts (with an elevated IFP of approximately 28 mmHg) and orthotopic human MCF7 breast tumours (with a notably lower IFP of approximately 14 mmHg), both before and during a long and slow period of GdDTPA perfusion. The method yielded parametric images of T_1 relaxation times and calculated the GdDTPA concentration at steady state. DCE-MRI data were correlated with an invasive wick-in-needle measurement of IFP. Typically, the concentration of GdDTPA showed a steep decline from the tumour rim towards the tumour centre. This pattern of distribution was not evident on histological sections for cell density or capillary density, and was therefore attributed to an increase in IFP, with those regions devoid of GdDTPA exhibiting the highest IFP. The method described could serve to map IFP and predict the presence of barriers to drug delivery. Obstacles to the clinical implementation of this technique ought to be few, as GdDTPA is already a widely used clinical contrast agent. Gulliksrud et al. (153) have also investigated the usefulness of DCE-MRI for the assessment of tumour IFP in A-07 and R-18 melanoma xenografts without necrosis. This study reported strong inverse correlations between $E \times F$ (where E is the initial extraction volume and F is the blood perfusion) and IFP for both tumour types, and between λ (λ is proportional to the extracellular volume fraction) and IFP in A-07 xenografts. This effect was not reproducible in tumours with necrotic regions. More recently, Hassid et al. (154) have used the same technique in human lung cancer xenografts to demonstrate a collagenase-induced increase in contrast agent delivery resulting from a decrease in IFP.

To our knowledge, Ferretti et al. (155) have thus far provided the only other example of the detection of drug-induced decreases in tumour IFP using DCE-MRI in conjunction with wick-in-needle methodology. DCE-MRI data were acquired for a wide variety of tumour models and used to calculate the relative tumour blood volume (rTBV) and an index of blood flow. Basal IFP was positively correlated with basal rTBV, but not at all with the index of blood flow. Treatment with cytostatic or cytotoxic agents decreased significantly the IFP of ectopic and orthotopic tumour models, and this paralleled the decreases in rTBV. In addition, rapid decreases in IFP preceded significant changes in tumour size. Overall, this in-depth study suggests that decreased tumour IFP could be a generic marker for a positive response to therapy.

An alternative way to evaluate the tumour extracellular fluid is by diffusion-weighted imaging (DWI), which measures the diffusivity of all the water content within the region of interest. DWI is affected by complex fluid motions within the tumour's many components, both intracellular and extracellular, and thus provides valuable information about the TME. The calculated apparent diffusion coefficient (ADC) is most commonly used to quantify the diffusivity of water, with high values indicating free diffusion and low values indicating restricted diffusion (156). The motion of water is more restricted in tissues with high cellularity and in intact cell membranes. Water can be thought of as being intravascular or extravascular; the extravascular water can be further divided into intra- and extracellular compartments, although it is important to remember that water will be exchanged between these compartments. There have been numerous theoretical models and experiments to try to determine the role played by each of these compartments in determining the ADC (157). The majority of these studies have examined changes in diffusion in relation to ischaemia, as this leads to a sudden and dramatic reduction in the ADC. Theoretically, by assuming that the intracellular compartment has a lower ADC, one can discriminate between the intra- and extravascular components. However, in vivo, these two ADC values are similar, and it is therefore difficult to distinguish between the different compartments (158).

Many studies have tried to alter the MR characteristics of a compartment, for example with relaxation agents or by altering the magnetic susceptibility (159,160). Others have evaluated the diffusion of MR-detectable molecules or ions that are restricted to and concentrated in a particular compartment. ^{19}F-Deoxyglucose-6-phosphate has been injected intravenously or into the lateral ventricles of rat brains to evaluate the intra- and extracellular compartments, respectively (158). Other exogenous molecules, including tetramethylammonium, mannitol and poly-ethylene glycol, have been used, as has the endogenous ion ^{23}Na (161–163). There have been no studies using such methods to evaluate solely the extracellular, extravascular fluid in response to therapy. In clinical practice, however, it is usually the conventional ADC of water molecules that is used to evaluate tumours and their surrounding tissue, i.e. peritumoral oedema.

Numerous studies in many tumour types have shown changes in DWI that correspond to response, in many cases very early after therapy. The outcome of DWI in numerous clinical trials has been reviewed recently (60). The main DWI finding in response to chemotherapy, radiotherapy and many of the newer therapies is that an early increase in ADC values predicts response and an improved outcome.

Early increases in ADC often precede any change in the tumour size, and may be used in the early assessment of response. This alteration in ADC after a response to therapy is thought to be a result of tumour cells undergoing lysis and necrosis, with a consequent decrease in cell membrane integrity and increased extracellular space, leading to an increase in the ADC (164). Many DWI studies have shown that low pretreatment ADC values predict patients who will respond better to treatment than those with high pretreatment ADC values (60). One explanation for this is that high ADC values are seen in necrotic tumours which are poorly perfused, hypoxic and acidotic, and therefore less sensitive to chemotherapy and radiotherapy.

With targeted therapies, particularly VDAs, the tumour volume can take weeks or months to alter, so that traditional imaging may not be the most accurate measure of response. DWI has been used in the early evaluation of a number of targeted therapies in xenograft models, including the VDA ZD6126, as mentioned earlier (36). Bevacizumab, a mAb that acts by blocking VEGF-A (VEGF-A stimulates angiogenesis), has been used successfully in the clinic to treat a range of tumours, including gliomas. A clinical trial by Rieger et al. (165) found that bevacizumab induced a

diffusion restriction (ADC decrease) as early as 4 weeks into therapy, which persisted for up to 80 weeks in 13 of 18 patients. In another trial, glioma patients treated with bevacizumab underwent DWI at 6 weeks and 3 months post-therapy; decreases in ADC in both the contrast-enhanced and noncontrast-enhanced parts of the lesion were seen in patients whose tumours went on to progress (166). Pope *et al.* (167) evaluated pretreatment ADC histogram analysis in patients with recurrent gliomas. They concluded that ADC values pretreatment could stratify more effectively progression-free survival in this group treated with bevacizumab than could enhancing tumour volume at first follow-up. Patients with less than mean ADC values had a 2.75-fold reduction in the median time to progression compared with patients with a higher than mean ADC value pretreatment. It is clear that the alteration in angiogenesis caused by bevacizumab can be measured by DWI; however, the reason for the reduction in ADC values seen after therapy remains unclear. It has been suggested that, as bevacizumab is an inhibitor of angiogenesis, it could induce atypical necrosis and chronic hypoxia (165).
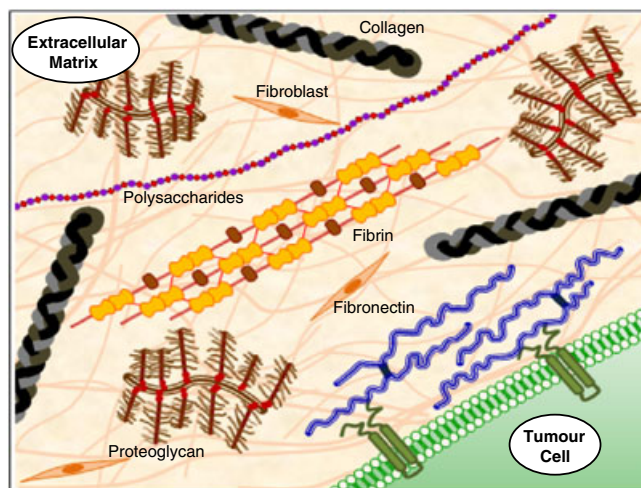

Figure 6. The extracellular matrix (ECM). The ECM provides structural support to the tumour cells. Stromal cells, including fibroblasts, secrete a variety of macromolecules into the ECM, creating a gel-like substance that acts as a stress absorber.

MRI OF THE ECM

As in all tissue types, the tumour ECM provides structural support for surrounding cells and is an important regulator of normal tissue behaviour and tissue homeostasis (4). The ECM contains various macromolecules that are secreted by tumour cells, fibroblasts and myofibroblasts. These ECM constituents include collagen, fibronectin, laminin, glycosaminoglycans, proteoglycans and glycoproteins, which create tensile strength, provide differentiation and survival signals, facilitate interactions between cells of different types and act as a physical scaffold for other ECM components (4,7). Together, these components contribute substantially to the biological characteristics of each tumour type, and represent an important alternative therapeutic target (Fig. 6). A number of MR techniques have been proposed for the detection of tissue macromolecular content, including magnetisation transfer imaging (MTI), $T_{1\rho}$ MRI and CEST. These methods provide a potential means of evaluating the effects of conventional chemotherapeutics on the ECM, as well as novel agents targeted specifically to components of the ECM.

Preclinical trials of MRI contrast agents targeted to the tumour matrix are currently underway, but are mainly limited to cancer biomarker detection rather than the assessment of biomarker response to therapeutic intervention. For example, Ye *et al.* (30) recently demonstrated the use of CTL1-(GdDTPA) to target tumour stromal fibrin–fibronectin complexes in human colon carcinoma xenografts. Variations on this methodology have been used to detect hyaluronidase activity (168), collagen content (169), transglutaminase activity (170) and fibroblast recruitment to the TME (171). However, as mentioned previously, the limited sensitivity of MRI detection and the high-level competing background signal limit this methodology to the detection of highly abundant target molecules, even when multiple gadolinium copies can be bound to the targeting peptide.

MMPs are a family of structurally related, multifunctional, zinc-dependent endopeptidases whose functions include the degradation of ECM proteins, cleavage of cell surface receptors and modulation of chemokine/cytokine activity. MMPs also have important functions in pathophysiologies characterised by excessive degradation of the ECM, such as rheumatoid arthritis, osteoarthritis, autoimmune blistering, and tumour invasion and

metastasis (9). MMPs are therefore potential biomarkers for cancer progression, invasiveness, angiogenesis and metastasis, e.g. mammary carcinoma (172) (Table 2).

The peptide chlorotoxin (CTX) binds preferentially to part of the membrane-bound matrix metalloproteinase-2 (MMP-2), which is up-regulated in a number of tumours, including glioma. CTX has been shown to be effective in targeting MNPs to 9L glioma xenografts (43,173). As well as binding to MMP-2, CTX inhibits tumour invasion, and therefore attachment of CTX peptides to MNPs is a promising potential treatment of glioma (174). A second peptide-conjugated contrast agent targeted to MMP-2 makes use of the PCA2-switch MMP-2 substrate, and has been preclinically validated in a mouse MC7-L1 mammary carcinoma xenograft model (172).

Quantification of MMP expression levels *in vivo* has not yet been achieved and, thus far, imaging results have been qualitative. In order to advance in the field of MMP MRI, and perform anti-MMP drug screening and monitor treatment efficacy, it will be important to correlate MMP expression levels with MRI data acquired with MMP-targeted contrast agents (175). Until recently, studies have failed to provide unequivocal evidence as to whether MMPs represent a drug target or antitarget. The clinical development of MMP inhibitors is now well underway, although selective MMP targeting is more likely to achieve clinical success than broadspectrum MMP inhibitors which can cause side-effects by hitting antitarget MMPs (9).

MTI is a popular noninvasive method of monitoring the TME, as it allows macromolecular protons of the ECM to be imaged indirectly. MTI was first described by Wolff and Balaban (176), and has been comprehensively reviewed by Henkelman *et al.* (177). Tsukushi *et al.* (178) have demonstrated significantly higher magnetisation transfer ratios (MTRs) in malignant compared with benign musculoskeletal tumours, and a statistically significant positive correlation between MTR and the DNA index. These results suggest that, alongside the DNA index, MTR can serve as a quantitative and noninvasive parameter to indicate musculoskeletal tumour malignancy and proliferative activity, and help plan diagnosis and treatment (178). The mean MTR has been shown to be statistically higher in biopsy-proven prostate malignancies of the peripheral

zone, compared with patients who tested negative for peripheral zone malignancy on biopsy (179), and a preliminary study has demonstrated that MTR can be used to differentiate benign from malignant breast lesions (180). However, MTR has also been shown to be lower in some tumour types, such as brain and parotid (181–184). In a study by Pui *et al.* (185), MTI was shown to differentiate between white matter, grey matter, infarct, and solid and cystic (infected) components of brain tumours in 107 patients. More recently, Yamamoto *et al.* (186) investigated whether MTR histogram analysis allows better detection than conventional MRI of early and subtle brain changes in patients with acute lymphocytic leukaemia who receive methotrexate therapy. MTR histogram peak height was significantly lower in post-chemotherapy scans than in pre-chemotherapy scans. This study demonstrates the use of MTR as an imaging biomarker for chemotherapy-induced changes in the brain, and its possible use for predicting central nervous system effects.

Another type of MTI that generates switchable negative contrast with no T_2^* effects is CEST. CEST can probe tissue via endogenous metabolites or injected contrast agents (79). APT imaging is a variant of CEST which specifically probes labile amide protons (187) in peptide bonds (188). Zhou *et al.* (188) have also demonstrated that APT imaging can distinguish between the tumour core and the contralateral normal-appearing white matter in patients with high-grade brain tumours, whereas APT intensities of contralateral normal-appearing white matter are indistinguishable from tumour in patients with low-grade brain tumours. APT intensities have also been successfully used to image heterogeneity in human brain tumours. For example, in a patient with glioblastoma multiforme, areas of necrosis and oedema exhibited lower APT signal intensities than the gadolinium-enhancing tumour core and cystic cavity (189). However, to our knowledge, these relatively new methods of generating MRI contrast have not yet been used as imaging biomarkers for tumour response to therapy.

$T_{1\rho}$ MRI is another contrast enhancement method that is sensitive to dipolar fluctuations in tissues which arise from slow atomic motions in viscous liquids and proteins (190); it has been investigated as an early indicator of therapeutic response to chemotherapy in the murine subcutaneous RIF-1 tumour model (191). $T_{1\rho}$ MRI data were acquired pre- and post-treatment with cyclophosphamide. Treated tumours exhibited a statistically significant percentage of pixels with prolonged $T_{1\rho}$ compared with untreated tumours. The percentage of pixels exhibiting prolonged $T_{1\rho}$ increased significantly 18 and 36 h after cyclophosphamide administration, whereas T_2 relaxation did not change significantly throughout this period. This study suggests that $T_{1\rho}$ MRI may be useful in evaluating early response to treatment with antitumour therapeutic regimes in the clinical setting. Sierra *et al.* (190) reported a statistically significant increase in $T_{1\rho}$ in BT4C glioma tissue corresponding to early changes in water dynamics induced by pro-apoptotic gene therapy.

CONCLUSIONS

Over the last few decades, it has become evident that tumours are not just composed of cancer cells and that many will not be cured by targeting therapy to cancer cells alone. The importance of the complex interaction between tumour cells and the surrounding matrix is gradually being evaluated. Traditional treatments for cancer, chemotherapy and radiotherapy, are designed to act directly on tumour cells. Newer targeted anticancer therapies not

only target the cancer cells, but have been rationally designed to target other components of the tumour, including the ECM, vasculature and stroma, that are essential for tumour development. As well as the structural elements of the tumour matrix, the physiological environment has a large role to play in the development of cancer. It has long been recognised that alterations in the physiological environment, such as hypoxia, have important implications for the way in which tumours respond to therapy. The evaluation of this aspect of the TME has the potential to allow the tailoring of therapy optimised to the physiological environment.

In this article, we have reviewed the imaging of physiological parameters, the response to therapy targeted towards the TME, and numerous and diverse targeted contrast agents for the detection of TME biomarkers by MRI and MRS. To allow the successful imaging of tumours and their microenvironment in response to therapy, we need to tailor the imaging to the therapy involved. Some therapies are cytostatic or antiangiogenic, whereas others are cytotoxic, and therefore the response to image will vary. The inclusion of MRI methods as biomarkers early in drug development is vital to ensure the progression of imaging into clinical practice.

In spite of evident preclinical successes, the relatively low sensitivity of MRI compared with alternative molecular imaging techniques has meant that targeted MRI contrast agents have often been administered at high and sometimes potentially toxic concentrations. Where this is not the case, *in vivo* efficacy has not always been demonstrated at clinically relevant field strengths. The use of MRI as a noninvasive, high-resolution anatomical/ molecular imaging technique to detect specific tumour biomarkers and to monitor the response to therapeutic intervention efficiently, reproducibly and with minimal adverse effects is a highly desirable prospect. However, it is obvious that, in order for clinical application and acceptance of these agents, efforts must be focused on the evolution of novel contrast agents or the improvement of amplification strategies to optimise SNR at lower, nontoxic doses.

For MRI of the TME to become routine in clinical practice, many of these methodologies and outcomes need to be standardised to allow comparison between sites and patients in large-scale clinical trials. Many of the MRI methods mentioned currently have a degree of subjectivity and consequential sampling error in the way that the ROI, voxel or single point of measurement is selected. This can have massive implications for correlation between *in vivo* noninvasive MRI and MRS data and *ex vivo* (often invasive) methods of measurement of pO_2, IFP, pH, etc. If imaging of the TME is to be used as a biomarker in clinical practice, it needs to be quantitative, reliable and accurate, as it will affect clinicians' decisions on therapy and therefore outcomes for individual patients. Quantitative measurements would allow a comparison between time points for the same patient and between different patients and institutions. Important questions to address when assessing the validity of any biomarker include: (1) is the response transient or sustained?; and (2) how well does the response correlate with current gold standards such as histology? The most important factor for patients is whether the result translates into an improvement in patient care and, therefore, overall survival.

and discussions throughout the preparation of the manuscript. Figure 3 was included with kind permission from AstraZeneca and Angiogene.

REFERENCES

1. Mueller MM, Fusenig NE. Friends or foes – bipolar effects of the tumour stroma in cancer. Nat. Rev. Cancer 2004; 4(11): 839–849.
2. Joyce JA. Therapeutic targeting of the tumor microenvironment. Cancer Cell 2005; 7(6): 513–520.
3. Weinberg RA. Coevolution in the tumor microenvironment. Nat. Genet. 2008; 40(5): 494–495.
4. Joyce JA, Pollard JW. Microenvironmental regulation of metastasis. Nat. Rev. Cancer 2009; 9(4): 239–252.
5. Mbeunkui F, Johann DJ Jr. Cancer and the tumor microenvironment: a review of an essential relationship. Cancer Chemother. Pharmacol. 2009; 63(4): 571–582.
6. Witz IP. The tumour microenvironment – introduction. Semin. Cancer Biol. 2002; 12(2): 87–88.
7. Kalluri R, Zeisberg M. Fibroblasts in cancer. Nat. Rev. Cancer 2006; 6(5): 392–401.
8. Nyalendo C, Sartelet H, Barrette S, Ohta S, Gingras D, Beliveau R. Identification of membrane-type 1 matrix metalloproteinase tyrosine phosphorylation in association with neuroblastoma progression. BMC Cancer 2009; 9: 422.
9. Vihinen P, Kahari VM. Matrix metalloproteinases in cancer: prognostic markers and therapeutic targets. Int. J. Cancer 2002; 99(2): 157–166.
10. Overall CM, Kleifeld O. Tumour microenvironment – opinion: validating matrix metalloproteinases as drug targets and anti-targets for cancer therapy. Nat. Rev. Cancer 2006; 6(3): 227–239.
11. Gillies RJ, Raghunand N, Karczmar GS, Bhujwalla ZM. MRI of the tumor microenvironment. J. Magn. Reson. Imaging 2002; 16(4): 430–450.
12. Penet MF, Glunde K, Jacobs MA, Pathak AP, Bhujwalla ZM. Molecular and functional MRI of the tumor microenvironment. J. Nucl. Med. 2008; 49(5): 687–690.
13. Cho H, Ackerstaff E, Carlin S, Lupu ME, Wang Y, Rizwan A, O'Donoghue J, Ling CC, Humm JL, Zanzonico PB, Koutcher JA. Noninvasive multimodality imaging of the tumor microenvironment: registered dynamic magnetic resonance imaging and positron emission tomography studies of a preclinical tumor model of tumor hypoxia. Neoplasia 2009; 11(3): 247–259, 242p following 259.
14. Glunde K, Jacobs MA, Pathak AP, Artemov D, Bhujwalla ZM. Molecular and functional imaging of breast cancer. NMR Biomed. 2009; 22(1): 92–103.
15. Padhani AR. Dynamic contrast-enhanced MRI in clinical oncology: current status and future directions. J. Magn. Reson. Imaging 2002; 16(4): 407–422.
16. Padhani AR. MRI for assessing antivascular cancer treatments. Br. J. Radiol. 2003; 76(Spec No 1): S60–S80.
17. O'Connor JP, Jackson A, Parker GJ, Jayson GC. DCE-MRI biomarkers in the clinical evaluation of antiangiogenic and vascular disrupting agents. Br. J. Cancer 2007; 96(2): 189–195.
18. Roberts C, Issa B, Stone A, Jackson A, Waterton JC, Parker GJ. Comparative study into the robustness of compartmental modeling and model-free analysis in DCE-MRI studies. J. Magn. Reson. Imaging 2006; 23(4): 554–563.
19. Tofts PS, Brix G, Buckley DL, Evelhoch JL, Henderson E, Knopp MV, Larsson HB, Lee TY, Mayr NA, Parker GJ, Port RE, Taylor J, Weisskoff RM. Estimating kinetic parameters from dynamic contrast-enhanced T(1)-weighted MRI of a diffusible tracer: standardized quantities and symbols. J. Magn. Reson. Imaging 1999; 10(3): 223–232.
20. Laking GR, West C, Buckley DL, Matthews J, Price PM. Imaging vascular physiology to monitor cancer treatment. Crit. Rev. Oncol. Hematol. 2006; 58(2): 95–113.
21. Veiseh O, Gunn JW, Zhang M. Design and fabrication of magnetic nanoparticles for targeted drug delivery and imaging. Adv. Drug Deliv. Rev. 2010; 62(3): 284–304.
22. Kohler N, Sun C, Fichtenholtz A, Gunn J, Fang C, Zhang M. Methotrexate-immobilized poly(ethylene glycol) magnetic nano-particles for MR imaging and drug delivery. Small 2006; 2(6): 785–792.
23. Jain TK, Morales MA, Sahoo SK, Leslie-Pelecky DL, Labhasetwar V. Iron oxide nanoparticles for sustained delivery of anticancer agents. Mol. Pharm. 2005; 2(3): 194–205.
24. Xiong XB, Ma Z, Lai R, Lavasanifar A. The therapeutic response to multifunctional polymeric nano-conjugates in the targeted cellular and subcellular delivery of doxorubicin. Biomaterials 2010; 31(4): 757–768.
25. Jain TK, Richey J, Strand M, Leslie-Pelecky DL, Flask CA, Labhasetwar V. Magnetic nanoparticles with dual functional properties: drug delivery and magnetic resonance imaging. Biomaterials 2008; 29(29): 4012–4021.
26. Medarova Z, Pham W, Farrar C, Petkova V, Moore A. In vivo imaging of siRNA delivery and silencing in tumors. Nat. Med. 2007; 13(3): 372–377.
27. Gore JC, Yankeelov TE, Peterson TE, Avison MJ. Molecular imaging without radiopharmaceuticals? J. Nucl. Med. 2009; 50(6): 999–1007.
28. Ackerstaff E, Glunde K, Bhujwalla ZM. Choline phospholipid metabolism: a target in cancer cells? J. Cell Biochem. 2003; 90(3): 525–533.
29. Glunde K, Bhujwalla ZM. Will magnetic resonance imaging (MRI)-based contrast agents for molecular receptor imaging make their way into the clinic? J. Cell. Mol. Med. 2008; 12(1): 187–188.
30. Ye F, Wu X, Jeong EK, Jia Z, Yang T, Parker D, Lu ZR. A peptide targeted contrast agent specific to fibrin–fibronectin complexes for cancer molecular imaging with MRI. Bioconjug. Chem. 2008; 19(12): 2300–2303.
31. Leach MO, Brindle KM, Evelhoch JL, Griffiths JR, Horsman MR, Jackson A, Jayson GC, Judson IR, Knopp MV, Maxwell RJ, McIntyre D, Padhani AR, Price P, Rathbone R, Rustin GJ, Tofts PS, Tozer GM, Vennart W, Waterton JC, Williams SR, Workman P. The assessment of antiangiogenic and antivascular therapies in early-stage clinical trials using magnetic resonance imaging: issues and recommendations. Br. J. Cancer 2005; 92(9): 1599–1610.
32. Morgan B, Thomas AL, Drevs J, Hennig J, Buchert M, Jivan A, Horsfield MA, Mross K, Ball HA, Lee L, Mietlowski W, Fuxuis S, Unger C, O'Byrne K, Henry A, Cherryman GR, Laurent D, Dugan M, Marme D, Steward WP. Dynamic contrast-enhanced magnetic resonance imaging as a biomarker for the pharmacological response of PTK787/ZK 222584, an inhibitor of the vascular endothelial growth factor receptor tyrosine kinases, in patients with advanced colorectal cancer and liver metastases: results from two phase I studies. J. Clin. Oncol. 2003; 21(21): 3955–3964.
33. Galbraith SM, Maxwell RJ, Lodge MA, Tozer GM, Wilson J, Taylor NJ, Stirling JJ, Sena L, Padhani AR, Rustin GJ. Combretastatin A4 phosphate has tumor antivascular activity in rat and man as demonstrated by dynamic magnetic resonance imaging. J. Clin. Oncol. 2003; 21(15): 2831–2842.
34. Robinson SP, McIntyre DJ, Checkley D, Tessier JJ, Howe FA, Griffiths JR, Ashton SE, Ryan AJ, Blakey DC, Waterton JC. Tumour dose response to the antivascular agent ZD6126 assessed by magnetic resonance imaging. Br. J. Cancer 2003; 88(10): 1592–1597.
35. McIntyre DJ, Robinson SP, Howe FA, Griffiths JR, Ryan AJ, Blakey DC, Peers IS, Waterton JC. Single dose of the antivascular agent, ZD6126 (N-acetylcolchinol-O-phosphate), reduces perfusion for at least 96 hours in the GH3 prolactinoma rat tumor model. Neoplasia 2004; 6(2): 150–157.
36. Vogel-Claussen J, Gimi B, Artemov D, Bhujwalla ZM. Diffusion-weighted and macromolecular contrast enhanced MRI of tumor response to antivascular therapy with ZD6126. Cancer Biol. Ther. 2007; 6(9): 1469–1475.
37. LoRusso PM, Gadgeel SM, Wozniak A, Barge AJ, Jones HK, DelProposto ZS, DeLuca PA, Evelhoch JL, Boerner SA, Wheeler C. Phase I clinical evaluation of ZD6126, a novel vascular-targeting agent, in patients with solid tumors. Invest. New Drugs 2008; 26(2): 159–167.
38. Lippert JW 3rd. Vascular disrupting agents. Bioorg. Med. Chem. 2007; 15(2): 605–615.
39. Robinson SP, Howe FA, Griffiths JR, Ryan AJ, Waterton JC. Susceptibility contrast magnetic resonance imaging determination of fractional tumor blood volume: a noninvasive imaging biomarker of response to the vascular disrupting agent ZD6126. Int. J. Radiat. Oncol. Biol. Phys. 2007; 69(3): 872–879.
40. McPhail LD, Griffiths JR, Robinson SP. Assessment of tumor response to the vascular disrupting agents 5,6-dimethylxanthenone-4-acetic acid or combretastatin-A4-phosphate by intrinsic susceptibility

magnetic resonance imaging. Int. J. Radiat. Oncol. Biol. Phys. 2007; 69(4): 1238–1245.

41. Howe FA, McPhail LD, Griffiths JR, McIntyre DJ, Robinson SP. Vessel size index magnetic resonance imaging to monitor the effect of antivascular treatment in a rodent tumor model. Int. J. Radiat. Oncol. Biol. Phys. 2008; 71(5): 1470–1476.

42. Varallyay CG, Muldoon LL, Gahramanov S, Wu YJ, Goodman JA, Li X, Pike MM, Neuwelt EA. Dynamic MRI using iron oxide nanoparticles to assess early vascular effects of antiangiogenic versus cortico-steroid treatment in a glioma model. J. Cereb. Blood Flow Metab. 2009; 29(4): 853–860.

43. Reddy GR, Bhojani MS, McConville P, Moody J, Moffat BA, Hall DE, Kim G, Koo YE, Woolliscroft MJ, Sugai JV, Johnson TD, Philbert MA, Kopelman R, Rehemtulla A, Ross BD. Vascular targeted nanopar-ticles for imaging and treatment of brain tumors. Clin. Cancer Res. 2006; 12(22): 6677–6686.

44. Brooks PC, Clark RA, Cheresh DA. Requirement of vascular integrin alpha v beta 3 for angiogenesis. Science 1994; 264(5158): 569–571.

45. Sipkins DA, Cheresh DA, Kazemi MR, Nevin LM, Bednarski MD, Li KC. Detection of tumor angiogenesis in vivo by alphaVbeta3-targeted magnetic resonance imaging. Nat. Med. 1998; 4(5): 623–626.

46. Winter PM, Caruthers SD, Kassner A, Harris TD, Chinen LK, Allen JS, Lacy EK, Zhang H, Robertson JD, Wickline SA, Lanza GM. Molecular imaging of angiogenesis in nascent Vx-2 rabbit tumors using a novel alpha(nu)beta3-targeted nanoparticle and 1.5 tesla magnetic resonance imaging. Cancer Res. 2003; 63(18): 5838–5843.

47. Schmieder AH, Winter PM, Caruthers SD, Harris TD, Williams TA, Allen JS, Lacy EK, Zhang H, Scott MJ, Hu G, Robertson JD, Wickline SA, Lanza GM. Molecular MR imaging of melanoma angiogenesis with alphanubeta3-targeted paramagnetic nanoparticles. Magn. Reson. Med. 2005; 53(3): 621–627.

48. Zhang C, Jugold M, Woenne EC, Lammers T, Morgenstern B, Mueller MM, Zentgraf H, Bock M, Eisenhut M, Semmler W, Kiessling F. Specific targeting of tumor angiogenesis by RGD-conjugated ultrasmall superparamagnetic iron oxide particles using a clinical 1.5-T magnetic resonance scanner. Cancer Res. 2007; 67(4): 1555–1562.

49. Montet X, Montet-Abou K, Reynolds F, Weissleder R, Josephson L. Nanoparticle imaging of integrins on tumor cells. Neoplasia 2006; 8 (3): 214–222.

50. Mulder WJ, Castermans K, van Beijnum JR, Oude Egbrink MG, Chin PT, Fayad ZA, Lowik CW, Kaijzel EL, Que I, Storm G, Strijkers GJ, Griffioen AW, Nicolay K. Molecular imaging of tumor angiogenesis using alphavbeta3-integrin targeted multimodal quantum dots. Angiogenesis 2009; 12(1): 17–24.

51. Zhang D, Feng XY, Henning TD, Wen L, Lu WY, Pan H, Wu X, Zou LG. MR imaging of tumor angiogenesis using sterically stabilized Gd-DTPA liposomes targeted to CD105. Eur. J. Radiol. 2009; 70(1): 180–189.

52. Oostendorp M, Douma K, Hackeng TM, Dirksen A, Post MJ, van Zandvoort MA, Backes WH. Quantitative molecular magnetic resonance imaging of tumor angiogenesis using cNGR-labeled paramagnetic quantum dots. Cancer Res. 2008; 68(18): 7676–7683.

53. de Vries IJ, Lesterhuis WJ, Barentsz JO, Verdijk P, van Krieken JH, Boerman OC, Oyen WJ, Bonenkamp JJ, Boezeman JB, Adema GJ, Bulte JW, Scheenen TW, Punt CJ, Heerschap A, Figdor CG. Magnetic resonance tracking of dendritic cells in melanoma patients for monitoring of cellular therapy. Nat. Biotechnol. 2005; 23(11): 1407–1413.

54. Daldrup-Link HE, Meier R, Rudelius M, Piontek G, Piert M, Metz S, Settles M, Uherek C, Wels W, Schlegel J, Rummeny EJ. In vivo tracking of genetically engineered, anti-HER2/neu directed natural killer cells to HER2/neu positive mammary tumors with magnetic resonance imaging. Eur. Radiol. 2005; 15(1): 4–13.

55. Hu DE, Kettunen MI, Brindle KM. Monitoring T-lymphocyte trafficking in tumors undergoing immune rejection. Magn. Reson. Med. 2005; 54(6): 1473–1479.

56. Sengar RS, Spokauskiene L, Steed DP, Griffin P, Arbujas N, Chambers WH, Wiener EC. Magnetic resonance imaging-guided adoptive cellular immunotherapy of central nervous system tumors with a T1 contrast agent. Magn. Reson. Med. 2009; 62(3): 599–606.

57. Leimgruber A, Berger C,Cortez-Retamozo V, Etzrodt M, Newton AP, Waterman P, Figueiredo JL, Kohler RH, Elpek N, Mempel TR, Swirski FK, Nahrendorf M, Weissleder R, Pittet MJ. Behavior of endogenous tumor-associated macrophages assessed in vivo using a

functionalized nanoparticle. Neoplasia 2009; 11(5): 459–468, 452p following 468.

58. Valable S, Barbier EL, Bernaudin M, Roussel S, Segebarth C, Petit E, Remy C. In vivo MRI tracking of exogenous monocytes/macro-phages targeting brain tumors in a rat model of glioma. Neuroimage 2007; 37(Suppl 1): S47–S58.

59. Beloueche-Babari M, Chung YL, Al-Saffar NM, Falck-Miniotis M, Leach MO. Metabolic assessment of the action of targeted cancer therapeutics using magnetic resonance spectroscopy. Br. J. Cancer 2010; 102(1): 1–7.

60. Marcus CD, Ladam-Marcus V, Cucu C, Bouche O, Lucas L, Hoeffel C. Imaging techniques to evaluate the response to treatment in oncology: current standards and perspectives. Crit. Rev. Oncol. Hematol. 2009; 72(3): 217–238.

61. Costello LC, Franklin RB, Narayan P. Citrate in the diagnosis of prostate cancer. Prostate 1999; 38(3): 237–245.

62. Kurhanewicz J, Swanson MG, Nelson SJ, Vigneron DB. Combined magnetic resonance imaging and spectroscopic imaging approach to molecular imaging of prostate cancer. J. Magn. Reson. Imaging 2002; 16(4): 451–463.

63. Costello LC, Franklin RB. Concepts of citrate production and secretion by prostate. 1. Metabolic relationships. Prostate 1991; 18 (1): 25–46.

64. Mueller-Lisse UG, Swanson MG, Vigneron DB, Hricak H, Bessette A, Males RG, Wood PJ, Noworolski S, Nelson SJ, Barken I, Carroll PR, Kurhanewicz J. Time-dependent effects of hormone-deprivation therapy on prostate metabolism as detected by combined magnetic resonance imaging and 3D magnetic resonance spec-troscopic imaging. Magn. Reson. Med. 2001; 46(1): 49–57.

65. Kimura T, Ohkubo M, Igarashi H, Kwee IL, Nakada T. Increase in glutamate as a sensitive indicator of extracellular matrix integrity in peritumoral edema: a 3.0-tesla proton magnetic resonance spectroscopy study. J. Neurosurg. 2007; 106(4): 609–613.

66. Lee SC, Poptani H, Pickup S, Jenkins WT, Kim S, Koch CJ, Delikatny EJ, Glickson JD. Early detection of radiation therapy response in non-Hodgkin's lymphoma xenografts by in vivo ^{1}H magnetic resonance spectroscopy and imaging.NMR Biomed. 2010; 23(6): 624–632.

67. Liimatainen T, Hakumaki JM, Kauppinen RA, Ala-Korpela M. Monitoring of gliomas in vivo by diffusion MRI and (1)H MRS during gene therapy-induced apoptosis: interrelationships be-tween water diffusion and mobile lipids. NMR Biomed. 2009; 22(3): 272–279.

68. Gade TP, Buchanan IM, Motley MW, Mazaheri Y, Spees WM, Koutcher JA. Imaging intratumoral convection: pressure-dependent enhancement in chemotherapeutic delivery to solid tumors. Clin. Cancer Res. 2009; 15(1): 247–255.

69. Gillies RJ, Liu Z, Bhujwalla Z. ^{31}P-MRS measurements of extracellular pH of tumors with 3-aminopropylphosphonate. Am. J. Physiol. 1994; 267(1 Pt 1): C195–C203.

70. Gil S, Zaderenzo P, Cruz F, Cerdan S, Ballesteros P. Imidazol-1-ylalkanoic acids as extrinsic ^{1}H NMR probes for the determination of intracellular pH, extracellular pH and cell volume. Bioorg. Med. Chem. 1994; 2(5): 305–314.

71. Ojugo AS, McSheehy PM, McIntyre DJ, McCoy C, Stubbs M, Leach MO, Judson IR, Griffiths JR. Measurement of the extracellular pH of solid tumours in mice by magnetic resonance spectroscopy: a comparison of exogenous (19)F and (31)P probes. NMR Biomed. 1999; 12(8): 495–504.

72. van Sluis R, Bhujwalla ZM, Raghunand N, Ballesteros P, Alvarez J, Cerdan S, Galons JP, Gillies RJ. In vivo imaging of extracellular pH using ^{1}H MRSI. Magn. Reson. Med. 1999; 41(4): 743–750.

73. Garcia-Martin ML, Herigault G, Remy C, Farion R, Ballesteros P, Coles JA, Cerdan S, Ziegler A. Mapping extracellular pH in rat brain gliomas in vivo by ^{1}H magnetic resonance spectroscopic imaging: comparison with maps of metabolites. Cancer Res. 2001; 61(17): 6524–6531.

74. Provent P, Benito M, Hiba B, Farion R, Lopez-Larrubia P, Ballesteros P, Remy C, Segebarth C, Cerdan S, Coles JA, Garcia-Martin ML. Serial in vivo spectroscopic nuclear magnetic resonance imaging of lactate and extracellular pH in rat gliomas shows redistribution of protons away from sites of glycolysis. Cancer Res. 2007; 67(16): 7638–7645.

75. Aime S, Delli Castelli D, Terreno E. Novel pH-reporter MRI contrast agents. Angew. Chem. Int. Ed. Engl. 2002; 41(22): 4334–4336.

76. Zhang S, Wu K, Sherry AD. A novel pH-sensitive MRI contrast agent. Angew. Chem. Int. Ed. Engl. 1999; 38(21): 3192–3194.

77. Aime S, Fedeli F, Sanino A, Terreno E. A R2/R1 ratiometric procedure for a concentration-independent, pH-responsive, Gd(III)-based MRI agent. J. Am. Chem. Soc. 2006; 128(35): 11 326–11 327.

78. Frullano L, Catana C, Benner T, Sherry AD, Caravan P. Bimodal MR-PET agent for quantitative pH imaging. Angew. Chem. Int. Ed. Engl. 2010; 49(13): 2382–2384.

79. Ward KM, Aletras AH, Balaban RS. A new class of contrast agents for MRI based on proton chemical exchange dependent saturation transfer (CEST). J. Magn. Reson. 2000; 143(1): 79–87.

80. Zhou J, Payen JF, Wilson DA, Traystman RJ, van Zijl PC. Using the amide proton signals of intracellular proteins and peptides to detect pH effects in MRI. Nat. Med. 2003; 9(8): 1085–1090.

81. Sun PZ, Sorensen AG. Imaging pH using the chemical exchange saturation transfer (CEST) MRI: correction of concomitant RF irradiation effects to quantify CEST MRI for chemical exchange rate and pH. Magn. Reson. Med. 2008; 60(2): 390–397.

82. Gallagher FA, Kettunen MI, Day SE, Hu DE, Ardenkjaer-Larsen JH, Zandt R, Jensen PR, Karlsson M, Golman K, Lerche MH, Brindle KM. Magnetic resonance imaging of pH in vivo using hyperpolarized ^{13}C-labelled bicarbonate. Nature 2008; 453(7197): 940–943.

83. Gillies RJ, Morse DL. In vivo magnetic resonance spectroscopy in cancer. Annu. Rev. Biomed. Eng. 2005; 7: 287–326.

84. Gillies RJ, Robey I, Gatenby RA. Causes and consequences of increased glucose metabolism of cancers. J. Nucl. Med. 2008; 49 (Suppl 2): 24S–42S.

85. Griffiths JR, McIntyre DJ, Howe FA, Stubbs M. Why are cancers acidic? A carrier-mediated diffusion model for H$^+$ transport in the interstitial fluid. Novartis Found. Symp. 2001; 240: 46–62; discussion 62–67, 152–153.

86. Fukumura D, Jain RK. Tumor microvasculature microenvironment targets antiangiogenesis normalization. Microvasc. Res. 2007; 74(2–3): 72–84.

87. Tredan O, Galmarini CM, Patel K, Tannock IF. Drug resistance and the solid tumor microenvironment. J. Natl Cancer Inst. 2007; 99(19): 1441–1454.

88. Gerweck LE, Seetharaman K. Cellular pH gradient in tumor versus normal tissue: potential exploitation for the treatment of cancer. Cancer Res. 1996; 56(6): 1194–1198.

89. Gerweck LE, Vijayappa S, Kozin S. Tumor pH controls the in vivo efficacy of weak acid and base chemotherapeutics. Mol. Cancer Ther. 2006; 5(5): 1275–1279.

90. Mahoney BP, Raghunand N, Baggett B, Gillies RJ. Tumor acidity, ion trapping and chemotherapeutics. I. Acid pH affects the distribution of chemotherapeutic agents in vitro. Biochem. Pharmacol. 2003; 66(7): 1207–1218.

91. Raghunand N, Mahoney BP, Gillies RJ. Tumor acidity, ion trapping and chemotherapeutics. II. pH dependent partition coefficients predict importance ion trapping pharmacokinetics weakly basic chemotherapeutic agents. Biochem. Pharmacol. 2003; 66(7): 1219–1229.

92. Kozin SV, Shkarin P, Gerweck LE. The cell transmembrane pH gradient in tumors enhances cytotoxicity of specific weak acid chemotherapeutics. Cancer Res. 2001; 61(12): 4740–4743.

93. Song CW. Effect of local hyperthermia on blood flow and microenvironment: a review. Cancer Res. 1984; 44(10 Suppl): 4721s–4730s.

94. Griffin RJ, Dings RP, Jamshidi-Parsian A, Song CW. Mild temperature hyperthermia and radiation therapy: role of tumour vascular thermotolerance and relevant physiological factors. Int. J. Hyperthermia 2010; 26(3): 256–263.

95. Rieke V, Butts Pauly K. MR thermometry. J. Magn. Reson. Imaging 2008; 27(2): 376–390.

96. Peller M, Kurze V, Loeffler R, Pahernik S, Dellian M, Goetz AE, Issels R, Reiser M. Hyperthermia induces T1 relaxation and blood flow changes in tumors. A MRI thermometry study in vivo. Magn. Reson. Imaging, 2003; 21(5): 545–551.

97. Dick EA, Joarder R, de Jode M, Taylor-Robinson SD, Thomas HC, Foster GR, Gedroyc WM. MR-guided laser thermal ablation of primary and secondary liver tumours. Clin. Radiol. 2003; 58(2): 112–120.

98. Martin RC 2nd. Intraoperative magnetic resonance imaging ablation of hepatic tumors. Am. J. Surg. 2005; 189(4): 388–394.

99. Gellermann J, Hildebrandt B, Issels R, Ganter H, Wlodarczyk W, Budach V, Felix R, Tunn PU, Reichardt P, Wust P. Noninvasive magnetic resonance thermography of soft tissue sarcomas during regional hyperthermia: correlation with response and direct thermometry. Cancer 2006; 107(6): 1373–1382.

100. Siddiqui K, Chopra R, Vedula S, Sugar L, Haider M, Boyes A, Musquera M, Bronskill M, Klotz L. MRI-guided transurethral ultrasound therapy of the prostate gland using real-time thermal mapping: initial studies. Urology 2010; 76(6): 1506–1511.

101. Mason RP. BOLD MRI: a tool for predicting tumour therapy outcome based on tumour blood oxygenation and vascular function. Imaging Med. 2009; 1(1): 11–13.

102. Al-Hallaq HA, Zamora M, Fish BL, Farrell A, Moulder JE, Karczmar GS. MRI measurements correctly predict the relative effects of tumor oxygenating agents on hypoxic fraction in rodent BA1112 tumors. Int. J. Radiat. Oncol. Biol. Phys. 2000; 47(2): 481–488.

103. Cooper RA, Carrington BM, Loncaster JA, Todd SM, Davidson SE, Logue JP, Luthra AD, Jones AP, Stratford I, Hunter RD, West CM. Tumour oxygenation levels correlate with dynamic contrast-enhanced magnetic resonance imaging parameters in carcinoma of the cervix. Radiother. Oncol. 2000; 57(1): 53–59.

104. Zhao JG, Feng GS, Kong XQ, Li X, Li MH, Cheng YS. Changes of tumor microcirculation after transcatheter arterial chemoembolization: first pass perfusion MR imaging and Chinese ink casting in a rabbit model. World J. Gastroenterol. 2004; 10(10): 1415–1420.

105. O'Connor JP, Naish JH, Parker GJ, Waterton JC, Watson Y, Jayson GC, Buonaccorsi GA, Cheung S, Buckley DL, McGrath DM, West CM, Davidson SE, Roberts C, Mills SJ, Mitchell CL, Hope L, Ton NC, Jackson A. Preliminary study of oxygen-enhanced longitudinal relaxation in MRI: a potential novel biomarker of oxygenation changes in solid tumors. Int. J. Radiat. Oncol. Biol. Phys. 2009; 75(4): 1209–1215.

106. Ogawa S, Lee TM, Nayak AS, Glynn P. Oxygenation-sensitive contrast in magnetic resonance image of rodent brain at high magnetic fields. Magn. Reson. Med. 1990; 14(1): 68–78.

107. Baudelet C, Gallez B. How does blood oxygen level-dependent (BOLD) contrast correlate with oxygen partial pressure (pO2) inside tumors? Magn. Reson. Med. 2002; 48(6): 980–986.

108. Fan X, River JN, Zamora M, Al-Hallaq HA, Karczmar GS. Effect of carbogen on tumor oxygenation: combined fluorine-19 and proton MRI measurements. Int. J. Radiat. Oncol. Biol. Phys. 2002; 54(4): 1202–1209.

109. Zhao D, Jiang L, Hahn EW, Mason RP. Comparison of ^{1}H blood oxygen level-dependent (BOLD) and ^{19}F MRI to investigate tumor oxygenation. Magn. Reson. Med. 2009; 62(2): 357–364.

110. Dunn JF, O'Hara JA, Zaim-Wadghiri Y, Lei H, Meyerand ME, Grinberg OY, Hou H, Hoopes PJ, Demidenko E, Swartz HM. Changes in oxygenation of intracranial tumors with carbogen: a BOLD MRI and EPR oximetry study. J. Magn. Reson. Imaging 2002; 16(5): 511–521.

111. Rijpkema M, Schuuring J, Bernsen PL, Bernsen HJ, Kaanders JH, van der Kogel AJ, Heerschap A. BOLD MRI response hypercapnic hyperoxia patients meningiomas correlation gadolinium DTPA uptake rate. Magn. Reson. Imaging 2004; 22(6): 761–767.

112. Griffiths JR, Taylor NJ, Howe FA, Saunders MI, Robinson SP, Hoskin PJ, Powell ME, Thoumine M, Caine LA, Baddeley H. The response of human tumors to carbogen breathing, monitored by gradient-recalled echo magnetic resonance imaging. Int. J. Radiat. Oncol. Biol. Phys. 1997; 39(3): 697–701.

113. Gross S, Gilead A, Scherz A, Neeman M, Salomon Y. Monitoring photodynamic therapy of solid tumors online by BOLD-contrast MRI. Nat. Med. 2003; 9(10): 1327–1331.

114. Zhao D, Jiang L, Hahn EW, Mason RP. Continuous low-dose (metronomic) chemotherapy on rat prostate tumors evaluated using MRI in vivo and comparison with histology. Neoplasia 2005; 7(7): 678–687.

115. Alonzi R, Padhani AR, Maxwell RJ, Taylor NJ, Stirling JJ, Wilson JI, d'Arcy JA, Collins DJ, Saunders MI, Hoskin PJ. Carbogen breathing increases prostate cancer oxygenation: a translational MRI study in murine xenografts and humans. Br. J. Cancer 2009; 100(4): 644–648.

116. Zhao D, Ran S, Constantinescu A, Hahn EW, Mason RP. Tumor oxygen dynamics: correlation of in vivo MRI with histological findings. Neoplasia 2003; 5(4): 308–318.

117. Kodibagkar VD, Cui W, Merritt ME, Mason RP. Novel ^{1}H NMR approach to quantitative tissue oximetry using hexamethyldisiloxane. Magn. Reson. Med. 2006; 55(4): 743–748.

118. Robinson SP, Griffiths JR. Current issues in the utility of ^{19}F nuclear magnetic resonance methodologies for the assessment of tumour

hypoxia. Philos. Trans. R. Soc. Lond. B. Biol. Sci. 2004; 359(1446): 987–996.

119. Aboagye EO, Maxwell RJ, Horsman MR, Lewis AD, Workman P, Tracy M, Griffiths JR. The relationship between tumour oxygenation determined by oxygen electrode measurements and magnetic resonance spectroscopy of the fluorinated 2-nitroimidazole SR-4554. Br. J. Cancer 1998; 77(1): 65–70.

120. Workman P, Maxwell RJ, Griffiths JR. Non-invasive MRS in new anticancer drug development. NMR Biomed. 1992; 5(5): 270–272.

121. Lord EM, Harwell L, Koch CJ. Detection of hypoxic cells by monoclonal antibody recognizing 2-nitroimidazole adducts. Cancer Res. 1993; 53(23): 5721–5726.

122. Seddon BM, Maxwell RJ, Honess DJ, Grimshaw R, Raynaud F, Tozer GM, Workman P. Validation of the fluorinated 2-nitroimidazole SR-4554 as a noninvasive hypoxia marker detected by magnetic resonance spectroscopy. Clin. Cancer Res. 2002; 8(7): 2323–2335.

123. Davda S, Bezabeh T. Advances in methods for assessing tumor hypoxia in vivo: implications for treatment planning. Cancer Metastasis Rev. 2006; 25(3): 469–480.

124. McIntyre DJO, McCoy CL, Griffiths JR. Tumour oxygenation measurements by F-19 magnetic resonance imaging of perfluorocarbons. Curr. Sci. 1999; 76(6): 753–762.

125. van der Sanden BP, Heerschap A, Simonetti AW, Rijken PF, Peters HP, Stuben G, van der Kogel AJ. Characterization and validation of noninvasive oxygen tension measurements in human glioma xenografts by ^{19}F-MR relaxometry. Int. J. Radiat. Oncol. Biol. Phys. 1999; 44(3): 649–658.

126. Noth U, Rodrigues LM, Robinson SP, Jork A, Zimmermann U, Newell B, Griffiths JR. In vivo determination of tumor oxygenation during growth and in response to carbogen breathing using 15C5-loaded alginate capsules as fluorine-19 magnetic resonance imaging oxygen sensors. Int. J. Radiat. Oncol. Biol. Phys. 2004; 60(3): 909–919.

127. Hunjan S, Mason RP, Constantinescu A, Peschke P, Hahn EW, Antich PP. Regional tumor oximetry: ^{19}F NMR spectroscopy of hexafluorobenzene. Int. J. Radiat. Oncol. Biol. Phys. 1998; 41(1): 161–171.

128. Zhao D, Jiang L, Mason RP. Measuring changes in tumor oxygenation. Meth. Enzymol. 2004; 386: 378–418.

129. Bourke VA, Zhao D, Gilio J, Chang CH, Jiang L, Hahn EW, Mason RP. Correlation of radiation response with tumor oxygenation in the Dunning prostate R3327-AT1 tumor. Int. J. Radiat. Oncol. Biol. Phys. 2007; 67(4): 1179–1186.

130. Maxwell RJ, Workman P, Griffiths JR. Demonstration of tumor-selective retention of fluorinated nitroimidazole probes by ^{19}F magnetic resonance spectroscopy in vivo. Int. J. Radiat. Oncol. Biol. Phys. 1989; 16(4): 925–929.

131. Aboagye EO, Kelson AB, Tracy M, Workman P. Preclinical development and current status of the fluorinated 2-nitroimidazole hypoxia probe N-(2-hydroxy-3,3,3-trifluoropropyl)-2-(2-nitro-1-imidazolyl) acetamide (SR 4554, CRC 94/17): a non-invasive diagnostic probe for the measurement of tumor hypoxia by magnetic resonance spectroscopy and imaging, and by positron emission tomography. Anticancer Drug Des. 1998; 13(6): 703–730.

132. Aboagye EO, Lewis AD, Graham MA, Tracy M, Kelson AB, Ryan KJ, Workman P. The pharmacokinetics, bioavailability and biodistribution in mice of a rationally designed 2-nitroimidazole hypoxia probe SR-4554. Anticancer Drug Des. 1996; 11(3): 231–242.

133. Aboagye EO, Lewis AD, Johnson A, Workman P, Tracy M, Huxham IM. The novel fluorinated 2-nitroimidazole hypoxia probe SR-4554: reductive metabolism and semiquantitative localisation in human ovarian cancer multicellular spheroids as measured by electron energy loss spectroscopic analysis. Br. J. Cancer 1995; 72(2): 312–318.

134. Aboagye EO, Maxwell RJ, Kelson AB, Tracy M, Lewis AD, Graham MA, Horsman MR, Griffiths JR, Workman P. Preclinical evaluation of the fluorinated 2-nitroimidazole N-(2-hydroxy-3,3,3-trifluoropropyl)-2-(2-nitro-1-imidazolyl) acetamide (SR-4554) as a probe for the measurement of tumor hypoxia. Cancer Res. 1997; 57(15): 3314–3318.

135. Aboagye EO, Lewis AD, Tracy M, Workman P. Bioreductive metabolism of the novel fluorinated 2-nitroimidazole hypoxia probe N-(2-hydroxy-3,3,3-trifluoropropyl)-2-(2-nitroimidazolyl) acetamide (SR-4554). Biochem. Pharmacol. 1997; 54(11): 1217–1224.

136. Seddon BM, Payne GS, Simmons L, Ruddle R, Grimshaw R, Tan S, Turner A, Raynaud F, Halbert G, Leach MO, Judson I, Workman P. A phase I study of SR-4554 via intravenous administration for noninvasive investigation of tumor hypoxia by magnetic resonance

spectroscopy in patients with malignancy. Clin. Cancer Res. 2003; 9(14): 5101–5112.

137. Lee CP, Payne GS, Oregioni A, Ruddle R, Tan S, Raynaud FI, Eaton D, Campbell MJ, Cross K, Halbert G, Tracy M, McNamara J, Seddon B, Leach MO, Workman P, Judson I. A phase I study of the nitroimidazole hypoxia marker SR4554 using ^{19}F magnetic resonance spectroscopy. Br. J. Cancer 2009; 101(11): 1860–1868.

138. Papadopoulou MV, Ji M, Bloomer WD. Novel fluorinated hypoxia-targeted compounds as non-invasive probes for measuring tumor-hypoxia by ^{19}F-magnetic resonance spectroscopy (^{19}F-MRS). Anticancer Res. 2006; 26(5A): 3253–3258.

139. Papadopoulou MV, Pouremad R, Bloomer WD, Wyrwicz A. Novel non-invasive probes for measuring tumor-hypoxia by ^{19}F-magnetic resonance spectroscopy (^{19}F-MRS). Studies in the SCCVII/C3H murine model. Anticancer Res. 2006; 26(5A): 3259–3263.

140. Procissi D, Claus F, Burgman P, Koziorowski J, Chapman JD, Thakur SB, Matei C, Ling CC, Koutcher JA. In vivo ^{19}F magnetic resonance spectroscopy and chemical shift imaging of tri-fluoro-nitroimidazole as a potential hypoxia reporter in solid tumors. Clin. Cancer Res. 2007; 13(12): 3738–3747.

141. Sentjurc M, Cemazar M, Sersa G. EPR oximetry of tumors in vivo in cancer therapy. Spectrochim. Acta A Mol. Biomol. Spectrosc. 2004; 60(6): 1379–1385.

142. Khan N, Williams BB, Hou H, Li H, Swartz HM. Repetitive tissue pO2 measurements by electron paramagnetic resonance oximetry: current status and future potential for experimental and clinical studies. Antioxid. Redox Signal 2007; 9(8): 1169–1182.

143. Swartz HM, Khan N, Buckey J, Comi R, Gould L, Grinberg O, Hartford A, Hopf H, Hou H, Hug E, Iwasaki A, Lesniewski P, Salikhov I, Walczak T. Clinical applications of EPR: overview and perspectives. NMR Biomed. 2004; 17(5): 335–351.

144. Khan N, Mupparaju S, Hekmatyar SK, Hou H, Lariviere JP, Demidenko E, Gladstone DJ, Kauppinen RA, Swartz HM. Effect of hyperoxygenation on tissue pO2 and its effect on radiotherapeutic efficacy of orthotopic F98 gliomas. Int. J. Radiat. Oncol. Biol. Phys. 2010; 78(4): 1193–1200.

145. Krishna MC, English S, Yamada K, Yoo J, Murugesan R, Devasahayam N, Cook JA, Golman K, Ardenkjaer-Larsen JH, Subramanian S, Mitchell JB. Overhauser enhanced magnetic resonance imaging for tumor oximetry: coregistration of tumor anatomy and tissue oxygen concentration. Proc. Natl Acad. Sci. U.S.A. 2002; 99(4): 2216–2221.

146. Matsumoto S, Yasui H, Batra S, Kinoshita Y, Bernardo M, Munasinghe JP, Utsumi H, Choudhuri R, Devasahayam N, Subramanian S, Mitchell JB, Krishna MC. Simultaneous imaging of tumor oxygenation and microvascular permeability using Overhauser enhanced MRI. Proc. Natl Acad. Sci. U.S.A. 2009; 106(42): 17 898–17 903.

147. Heldin CH, Rubin K, Pietras K, Ostman A. High interstitial fluid pressure – an obstacle in cancer therapy. Nat. Rev. Cancer 2004; 4(10): 806–813.

148. Ozerdem U. Measuring interstitial fluid pressure with fiberoptic pressure transducers. Microvasc. Res. 2009; 77(2): 226–229.

149. Haider MA, Sitartchouk I, Roberts TP, Fyles A, Hashmi AT, Milosevic M. Correlations between dynamic contrast-enhanced magnetic resonance imaging-derived measures of tumor microvasculature and interstitial fluid pressure in patients with cervical cancer. J. Magn. Reson. Imaging 2007; 25(1): 153–159.

150. Lyng H, Tufto I, Skretting A, Rofstad EK. Proton relaxation times interstitial fluid pressure human melanoma xenografts. Br. J. Cancer 1997; 75(2): 180–183.

151. Milosevic M, Fyles A, Hill R. Interstitial fluid pressure in cervical cancer: guide to targeted therapy. Am. J. Clin. Oncol. 2001; 24(5): 516–521.

152. Hassid Y, Furman-Haran E, Margalit R, Eilam R, Degani H. Noninvasive magnetic resonance imaging of transport and interstitial fluid pressure in ectopic human lung tumors. Cancer Res. 2006; 66(8): 4159–4166.

153. Gulliksrud K, Brurberg KG, Rofstad EK. Dyn. contrast enhanced magnetic resonance imaging tumor interstitial fluid pressure. Radiother. Oncol. 2009; 91(1): 107–113.

154. Hassid Y, Eyal E, Margalit R, Furman-Haran E, Degani H. Non-invasive imaging of barriers to drug delivery in tumors. Microvasc. Res. 2008; 76(2): 94–103.

155. Ferretti S, Allegrini PR, Becquet MM, McSheehy PM. Tumor interstitial fluid pressure as an early-response marker for anticancer therapeutics. Neoplasia 2009; 11(9): 874–881.

156. Cercignani M, Horsfield MA. The physical basis of diffusion-weighted MRI. J. Neurol. Sci. 2001; 186(Suppl 1): S11–S14.

157. Norris DG. The effects of microscopic tissue parameters on the diffusion weighted magnetic resonance imaging experiment. NMR Biomed. 2001; 14(2): 77–93.

158. Duong TQ, Ackerman JJ, Ying HS, Neil JJ. Evaluation of extra- and intracellular apparent diffusion in normal and globally ischemic rat brain via ^{19}F NMR. Magn. Reson. Med. 1998; 40(1): 1–13.

159. Quirk JD, Bretthorst GL, Duong TQ, Snyder AZ, Springer CS Jr, Ackerman JJ, Neil JJ. Equilibrium water exchange between the intra- extracellular spaces mammalian brain. Magn. Reson. Med. 2003; 50(3): 493–499.

160. Silva MD, Omae T, Helmer KG, Li F, Fisher M, Sotak CH. Separating changes in the intra- and extracellular water apparent diffusion coefficient following focal cerebral ischemia in the rat brain. Magn. Reson. Med. 2002; 48(5): 826–837.

161. Goodman JA, Kroenke CD, Bretthorst GL, Ackerman JJ, Neil JJ. Sodium ion apparent diffusion coefficient in living rat brain. Magn. Reson. Med. 2005; 53(5): 1040–1045.

162. Duong TQ, Sehy JV, Yablonskiy DA, Snider BJ, Ackerman JJ, Neil JJ. Extracellular apparent diffusion in rat brain. Magn. Reson. Med. 2001; 45(5): 801–810.

163. Kroenke CD, Ackerman JJ, Neil JJ. Magnetic resonance measurement of tetramethylammonium diffusion in rat brain: comparison of magnetic resonance and ionophoresis in vivo diffusion measurements. Magn. Reson. Med. 2003; 50(4): 717–726.

164. Moffat BA, Hall DE, Stojanovska J, McConville PJ, Moody JB, Chenevert TL, Rehemtulla A, Ross BD. Diffusion imaging for evaluation of tumor therapies in preclinical animal models. MAGMA 2004; 17(3–6): 249–259.

165. Rieger J, Bähr O, Müller K, Franz K, Steinbach J, Hattingen E. Bevacizumab-induced diffusion-restricted lesions in malignant glioma patients. J. Neurooncol. 2010; 99(1): 49–56.

166. Jain R, Scarpace LM, Ellika S, Torcuator R, Schultz LR, Hearshen D, Mikkelsen T. Imaging response criteria for recurrent gliomas treated with bevacizumab role of diffusion weighted imaging as an imaging biomarker. J. Neurooncol. 2010; 96(3): 423–431.

167. Pope WB, Kim HJ, Huo J, Alger J, Brown MS, Gjertson D, Sai V, Young JR, Tekchandani L, Cloughesy T, Mischel PS, Lai A, Nghiemphu P, Rahmanuddin S, Goldin J. Recurrent glioblastoma multiforme: ADC histogram analysis predicts response to bevacizumab treatment. Radiology 2009; 252(1): 182–189.

168. Shiftan L, Israely T, Cohen M, Frydman V, Dafni H, Stern R, Neeman M. Magnetic resonance imaging visualization of hyaluronidase in ovarian carcinoma. Cancer Res. 2005; 65(22): 10 316–10 323.

169. Helm PA, Caravan P, French BA, Jacques V, Shen L, Xu Y, Beyers RJ, Roy RJ, Kramer CM, Epstein FH. Postinfarction myocardial scarring in mice: molecular MR imaging with use of a collagen-targeting contrast agent. Radiology 2008; 247(3): 788–796.

170. Mazooz G, Mehlman T, Lai TS, Greenberg CS, Dewhirst MW, Neeman M. Development of magnetic resonance imaging contrast material for in vivo mapping of tissue transglutaminase activity. Cancer Res. 2005; 65(4): 1369–1375.

171. Granot D, Addadi Y, Kalchenko V, Harmelin A, Kunz-Schughart LA, Neeman M. In vivo imaging of the systemic recruitment of fibroblasts to the angiogenic rim of ovarian carcinoma tumors. Cancer Res. 2007; 67(19): 9180–9189.

172. Lebel R, Jastrzebska B, Therriault H, Cournoyer MM, McIntyre JO, Escher E, Neugebauer W, Paquette B, Lepage M. Novel solubility-switchable MRI agent allows the noninvasive detection of matrix metalloproteinase-2 activity in vivo in a mouse model. Magn. Reson. Med. 2008; 60(5): 1056–1065.

173. Sun C, Veiseh O, Gunn J, Fang C, Hansen S, Lee D, Sze R, Ellenbogen RG, Olson J, Zhang M. In vivo MRI detection of gliomas by chlorotoxin-conjugated superparamagnetic nanoprobes. Small 2008; 4(3): 372–379.

174. Deshane J, Garner CC, Sontheimer H. Chlorotoxin inhibits glioma cell invasion via matrix metalloproteinase-2. J. Biol. Chem. 2003; 278(6): 4135–4144.

175. Cai W, Rao J, Gambhir SS, Chen X. How molecular imaging is speeding up antiangiogenic drug development. Mol. Cancer Ther. 2006; 5(11): 2624–2633.

176. Wolff SD, Balaban RS. Magnetization transfer contrast (MTC) and tissue water proton relaxation in vivo. Magn. Reson. Med. 1989; 10(1): 135–144.

177. Henkelman RM, Stanisz GJ, Graham SJ. Magnetization transfer in MRI: a review. NMR Biomed. 2001; 14(2): 57–64.

178. Tsukushi S, Takahashi M, Miyagi N, Matsushima S, Andoh M, Kinosada Y. Magnetization transfer ratios of musculoskeletal tumors. J. Orthop. Sci. 2002; 7(5): 524–527.

179. Kumar V, Jagannathan NR, Kumar R, Thulkar S, Gupta SD, Hemal AK, Gupta NP. Evaluation role of the magnetization transfer imaging prostate in preliminary study. Magn. Reson. Imaging 2008; 26(5): 644–649.

180. Bonini RH, Zeotti D, Saraiva LA, Trad CS, Filho JM, Carrara HH, de Andrade JM, Santos AC, Muglia VF. Magnetization transfer ratio as a predictor of malignancy in breast lesions: preliminary results. Magn. Reson. Med. 2008; 59(5): 1030–1034.

181. Takashima S, Wang J, Takayama F, Momose M, Matsushita T, Kawakami S, Saito A, Ishiyama T. Parotid masses: prediction of malignancy using magnetization transfer and MR imaging findings. Am. J. Roentgenol. 2001; 176(6): 1577–1584.

182. Okumura A, Takenaka K, Nishimura Y, Asano Y, Sakai N, Kuwata K, Era S. The characterization of human brain tumor using magnetization transfer technique in magnetic resonance imaging. Neurol. Res. 1999; 21(3): 250–254.

183. Boorstein JM, Wong KT, Grossman RI, Bolinger L, McGowan JC. Metastatic lesions of the brain: imaging with magnetization transfer. Radiology 1994; 191(3): 799–803.

184. Yousem DM, Schnall MD, Dougherty L, Weinstein GS, Hayden RE. Magnetization transfer imaging of the head and neck: normative data. Am. J. Neuroradiol. 1994; 15(6): 1117–1121.

185. Pui MH. Magnetization transfer analysis of brain tumor, infection, and infarction. J. Magn. Reson. Imaging 2000; 12(3): 395–399.

186. Yamamoto A, Miki Y, Adachi S, Kanagaki M, Fushimi Y, Okada T, Kobayashi M, Hiramatsu H, Umeda K, Nakahata T, van Buchem MA, Togashi K. Whole brain magnetization transfer histogram analysis of pediatric acute lymphoblastic leukemia patients receiving intrathecal methotrexate therapy. Eur. J. Radiol. 2006; 57(3): 423–427.

187. Sun PZ. Simultaneous determination of labile proton concentration and exchange rate utilizing optimal RF power: radio frequency power (RFP) dependence of chemical exchange saturation transfer (CEST) MRI. J. Magn. Reson. 2009; 202(2): 155–161.

188. Zhou J, Blakeley JO, Hua J, Kim M, Laterra J, Pomper MG, van Zijl PC. Practical data acquisition method for human brain tumor amide proton transfer (APT) imaging. Magn. Reson. Med. 2008; 60(4): 842–849.

189. Wen Z, Hu S, Huang F, Wang X, Guo L, Quan X, Wang S, Zhou J. MR imaging of high-grade brain tumors using endogenous protein and peptide-based contrast. Neuroimage 2010; 51(2): 616–622.

190. Sierra A, Michaeli S, Niskanen JP, Valonen PK, Grohn HI, Yla-Herttuala S, Garwood M, Grohn OH. Water spin dynamics during apoptotic cell death in glioma gene therapy probed by T1rho and T2rho. Magn. Reson. Med. 2008; 59(6): 1311–1319.

191. Duvvuri U, Poptani H, Feldman M, Nadal-Desbarats L, Gee MS, Lee WM, Reddy R, Leigh JS, Glickson JD. Quantitative T1rho magnetic resonance imaging of RIF-1 tumors in vivo: detection of early response to cyclophosphamide therapy. Cancer Res. 2001; 61(21): 7747–7753.

Copyright © 2011 John Wiley & Sons, Ltd.